



Statistical Physics of Complex Systems | (SMR 3624)

08 Sep 2021 - 10 Sep 2021
Virtual, Virtual, Italy

P01 - AIT EL DJOUDI Amal

Comparison of the Projected Color-singlet Partition Function of the QGP Calculated Within Different Terms in the Density of States

P02 - BAB Alejandra Marisa

Frustration in coupled magnetic thin films due to competition between exchange and dipolar interactions.

P03 - BISWAS Ayan

Information dynamics as a potential predictive tool for fluctuation-control in recurrent feed-forward architectures

P04 - CABRERA Juan Luis

Criticality and the fractal structure of $-5/3$ turbulent cascades

P05 - CARUSELA Florencia Maria

Antiresonant driven systems for particle manipulation

P06 - CHAUDHARY Ashok

Electrically switchable and optically tunable silicone oil/liquid crystal based complex emulsion system for optical device applications

P07 - COGHI Francesco

Role of current fluctuations in nonreversible samplers

P08 - ENCINAS RIVEROS Jesus Mauricio

Fundamental ingredients for discontinuous phase transitions in the inertial majority vote model

P09 - FABRIS Fiorella

Intermittent oscillations in Embryonic Stem Cells

P10 - GANCIO VAZQUEZ Juan

Approximating the resistance distance and eigenvector centrality from the network's eigenvalues

P11 - GANDICA Yérali

Signs of universal patterns in social explosions

P12 - GHOULI Zakaria

On the performance of a flow energy harvester using time delay

P13 - GRASSBERGER Peter

Markovian Anticipation in PERM simulations of high-dimensional SAWs: A study of guidance in rare-even simulations for non-Markovian systems

P14 - GUTIÉRREZ Caracé

Observation of bifurcations and hysteresis in experimentally coupled logistic maps

P15 - HARUNARI Eduardo Pedro

Entropy production fluctuation in phase transitions

P16 - ILIC Milan Velimir

Generalized Hamiltonian mean-field models

P17 - IRANNEZHAD Ali

Study of aging and failure using lifetime statistics of thin liquid films

P18 - KARIMI RIZI Abbas

Epidemic Spreading and Digital Contact Tracing: Effects of Heterogeneous Mixing and Quarantine Failures

P19 - K C Ahmed Niyaz

Magnetic properties of BaCuTe₂O₆

P20 - KENT-DOBIAS Patrick Jaron

Analytic continuation over complex landscapes

P21 - KORBEL Jan

Thermodynamics of structure-forming systems

P22 - LOOS A.M. Sarah

Irreversibility, heat and information flows induced by non-reciprocal interactions

P23 - MANZANO PAULE Gonzalo

Thermodynamics of Gambling Demons

P24 - MASROUR Rachid

Study of electronic, magnetic and magnetocaloric properties of double perovskites

P25 - MIDHA Tripti

Asymmetric coupling of two-channel exclusion process with interactions

P26 - MISHRA Kumar Pramod

Adsorption of a confined polymer chain: Exact results

P27 - MORAES Teixeira De Juliane

Study of time series of epidemic prevalence using the visibility graph.

P28 - MORENO Pérez Nahuel

A different way to analyze model membranes

P29 - MOUSSAOUI Bachir

The quark number susceptibility near the critical transition point in the Phase Transition from a hadronic gas to a colorless QCD plasma

P30 - PHAM Minh Tuan

Explaining Balanced Triad Statistics in Society by Dyadic Interactions

P31 - PONCET Alexis

Non-reciprocal mechanics of crystals violating Newton's third law

P32 - RAO Priyanka Nitin

Structure of Wavefunction for Many-Boson Systems in Mean-Field with Random k-Body Interactions

P33 - SALIERNO Gabriel

Liquid-Solid fluidized bed CFD-DEM simulation and validation by Radioactive Particle Tracking

P34 - SANTRA Ion

Direction reversing active Brownian particles

P35 - SARACCO Pablo Gustavo

Critical Behavior of the Ising Model under an external shear field: The Conserved Case

P36 - SARKAR Mrinal

Nonequilibrium tricritical point in the Kuramoto model with additional nearest-neighbor interactions

P37 - SCHÖNSBERG Francesca

Continuous quasi-attractors for irregular memories

P38 - SENYANGE Bob

Chaotic behavior of disordered nonlinear lattices

P39 - TOPAL KEMENT İrem

Network Reconstruction from Data

P40 - VENTURELLI Davide

Dynamics of probe particles in near-critical fields

P41 - WALTER Benjamin

Dragged colloids in (active) fields

P42 - WILLY ANISET Nganfo Yifoue

Probability density of bipolaron in a parabolic potential two-dimensional quantum dot under external magnetic and electric fields

P43 - YAN Jin

Distinguished correlation properties of Chebyshev dynamical systems

P44 - ZAMORA Javier Dario

Solving the Poles of Nonextensive Statistical Physics

Comparison of the Projected Color-singlet Partition Function of the QGP Calculated Within Different Terms in the Density of States

The present work deals with the study of hadronic matter at extreme conditions of temperature and/or baryonic density, where quarks and gluons are expected to be in a deconfined state called Quark-Gluon Plasma (QGP). According to the color confinement which is one of the main properties of Quantum Chromodynamics (QCD), this QGP may be in a color-singlet state. We account for such a requirement by projecting the partition function of the QGP on the color-singlet SU(3) representation using the projection technique. The density of states used in the calculation is that given by the Multiple Reflection Expansion (MRE) approximation, where the surface and curvature terms are considered additionally to the volume term, for the case of a QGP consisting of gluons and massless u and d quarks and s quarks. We study the influence of considering the curvature term, as well as the surface one on the obtained color-singlet partition functions and on some related physical quantities characterizing the QGP phase of matter and we compare the obtained results to previous results obtained in the absence of the contribution of the curvature and area terms to the density of states.

Frustration in coupled magnetic thin films due to competition between exchange and dipolar interactions.

The observation of alternated strip magnetic domains in monolayered films has been reported when perpendicular anisotropy is present. The case of a strong perpendicular anisotropy (SPA) has been modelled by the 2d-ferromagnetic Ising model adding dipolar interactions. This term induces frustration due to the competition with the exchange interaction, so structures with net zero magnetization appear. The phase diagram exhibits many phases and transitions of different kind. At low temperatures, antiferromagnetic and alternated spin stripes of width h emerge, where h increases with the exchange and dipolar constant ratio $\delta=J/g$. At higher temperatures, a tetragonal-liquid phase (TL) takes place, where the spin stripes intersect perpendicularly. Furthermore, it was found an intermediate nematic phase for $\delta > 2$. The phase transitions can be first, second order or the Kosterlitz-Thouless type. On the other hand, when two ferromagnetic SPA films are separated by a nonmagnetic layer, the interlayer coupling is RKKY like, i.e., presents a damped oscillation from ferro to antiferromagnetic with the thickness of the nonmagnetic layer. This fact leads to a complex phase behavior, whose study by means of Monte Carlo simulations is the goal of this work. For doing this, the exchange and dipolar constants are fixed to obtain stripes with different width on each film, and the interlayer coupling is varied to have a ferro or antiferromagnetic interaction. The equilibrium configurations at different temperatures and the phase transitions are characterized and compared in relation to the respective monolayer phase behavior for the same values of δ .

Information dynamics as a potential predictive tool for fluctuation-control in recurrent feed-forward architectures

In the last decade, bioinformatic analyses have found several small-scale network patterns which appear with appreciable statistical abundances in bacterial gene-transcription networks. The coherent type-1 feed-forward loop (C1-FFL) motif is one of such interaction patterns which plays crucial roles in the metabolic and chemotactic activities of the model organism *E. coli*. Hence, a clear and simultaneous understanding of the information processing and noise propagation in this abundant motif is of prime importance from the standpoint of network evolution. We use the metric of multivariate transfer entropy to evaluate the unique, synergistic and redundant features of the dynamic information which flows from the transcriptional regulators (predictors) to their jointly enslaved gene-product (target). Our approximate analytical estimates which are obtained within the small noise regime and further validated by exact Langevin stochastic simulation demonstrate that the synergistic and redundant information transfers are anti-correlated with the noise level of the output gene-product. Moreover, the former two information transfers are maximized before the output fluctuations become minimum and then begin to rise. We verify these findings under sufficiently broad regime of biologically relevant parameterization in order to hypothesize that the synergistic and redundant information transfers can act as suitable predictors for the output gene-expression noise. The generic C1-FFL construct is empowered with tunable direct and indirect regulatory control over the output gene-product so that various instances of the network motif may be compared in terms of their information/fluctuation transduction capabilities. Therefore, predictive insights about the interconnections between network topologies and information dynamics are obtained.

Criticality and the fractal structure of $-5/3$ turbulent cascades

Here we show a procedure to generate an analytical structure producing a cascade that scales as the energy spectrum in isotropic homogeneous turbulence. We obtain a function that unveils a non-self-similar fractal at the origin of the cascade. It reveals that the backbone underlying $-5/3$ cascades is formed by deterministic nested polynomials with parameters tuned in a Hopf bifurcation critical point. The cascade scaling is exactly obtainable (not by numerical simulations) from deterministic low dimensional nonlinear dynamics. Consequently, it should not be exclusive for fluids but also present in other complex phenomena. The scaling is obtainable both in deterministic and stochastic situations.

P05

Antiresonant driven systems for particle manipulation

Electrically switchable and optically tunable silicone oil/liquid crystal based complex emulsion system for optical device applications

In this study, we have reported a new approach for dynamic response to reconfigure the complex colloidal systems. The liquid crystals community which still looking for promising new directions for advancement of liquid crystal applications beyond display one. For this nanotemplate, nanomaterials and complex colloidal systems are already using to explore liquid crystals potentials. The recent findings which still not explored well and many possibilities to address the unsolved brainteasers motivate us to perform these investigations. Here, we are presenting the three different colloidal systems i.e. ethanol, water and silicone oil using with nematic liquid crystal (8CB) to form different emulsion systems to tune high electrical and optical properties. From these three different emulsions systems, LC/silicone oil complex system proves a very stable configuration with optimized concentration. The stable droplet morphology with dynamic switching has been demonstrated through LC/silicone oil emulsion in respect of other emulsions. In addition to this, a very nice optical properties has been achieved through this emulsion system that show LC director field controlled well through each LC/silicone oil interface. This enhancement in optical properties attributes to boundary conditions as well, which allow us to create topological deformations as influential prototype for accurate configuration near the droplet interface. These results are revealing the controlled morphological dynamics of complex LC/silicone oil colloidal systems make a potential candidate for electrical switchable and optically tunable rich soft material platform which can be used in photonics, metamaterials, sensing and liquid crystals elastomers applications.

Role of current fluctuations in nonreversible samplers

It is known that the distribution of nonreversible Markov processes breaking the detailed balance condition converges faster to the stationary distribution compared to reversible processes having the same stationary distribution. This is used in practice to accelerate Markov chain Monte Carlo algorithms that sample the Gibbs distribution by adding nonreversible transitions or non-gradient drift terms. The breaking of detailed balance also accelerates the convergence of empirical estimators to their ergodic expectation in the long-time limit. In this poster, we give a physical interpretation of this second form of acceleration in terms of currents associated with the fluctuations of empirical estimators using the level 2.5 of large deviations, which characterises the likelihood of density and current fluctuations in Markov processes. Focusing on diffusion processes, we show that there is accelerated convergence because estimator fluctuations arise in general with current fluctuations, leading to an added large deviation cost compared to the reversible case, which shows no current. We illustrate these results for the Ornstein-Uhlenbeck process in two dimensions.

Fundamental ingredients for discontinuous phase transitions in the inertial majority vote model

Discontinuous transitions have received considerable interest due to the uncovering that many phenomena such as catastrophic changes, epidemic outbreaks and synchronization present a behavior signed by abrupt (macroscopic) changes (instead of smooth ones) as a tuning parameter is changed. However, in different cases there are still scarce microscopic models reproducing such above trademarks. With these ideas in mind, we investigate the key ingredients underpinning the discontinuous transition in one of the simplest systems with up-down Z_2 symmetry recently ascertained in [Phys. Rev. E 95, 042304 (2017)]. Such system, in the presence of an extra ingredient-the inertia- has its continuous transition being switched to a discontinuous one in complex networks. We scrutinize the role of three central ingredients: inertia, system degree, and the lattice topology. Our analysis has been carried out for regular lattices and random regular networks with different node degrees (interacting neighborhood) through mean-field theory (MFT) treatment and numerical simulations. Our findings reveal that not only the inertia but also the connectivity constitute essential elements for shifting the phase transition. Astoundingly, they also manifest in low-dimensional regular topologies, exposing a scaling behavior entirely different than those from the complex networks case. Therefore, our findings put on firmer bases the essential issues for the manifestation of discontinuous transitions in such relevant class of systems with Z_2 symmetry.

Intermittent oscillations in Embryonic Stem Cells

Embryonic stem cells are pluripotent cells capable of generating every cell type in the body through differentiation programs, usually driven by extracellular signals. Signal transduction networks processes these signals, and can generate characteristic dynamic activities that are shaped by their cell-type specific architecture. The dynamic activities of target proteins rule the DNA expression that ends on activating the differentiation programs. The stimulus that controls the differentiation of pluripotent cells is known, but the dynamic activity that encodes this information remains unexplored. Here we are interested in how the information carried by these external inputs is encoded by the cell in signaling networks activity in mouse embryonic stem cells. We measured the dynamic activity of a target protein in single cells under ligand stimulation, and we present a characterization of the signalling dynamics that arises from time series analysis. We developed a set of local observables to explore how the extracellular stimulus concentrations correlate with signaling dynamic signatures, and tested the hypothesis that arose from this analysis. We found that the target protein activity is pulsatile in embryonic stem cells. Our analysis shows that single cells can transit between oscillatory and non-oscillatory behavior, leading to heterogeneous dynamic activities in the population. Oscillations become more prevalent with increasing ligand dose, while maintaining a robust characteristic timescale. Our results suggest that the signalling system operates in the vicinity of a transition point between oscillatory and non-oscillatory dynamics. Currently, we are trying to find a theoretical description of this system.

Approximating the resistance distance and eigenvector centrality from the network's eigenvalues

There are different measures to classify a network's data set that, depending on the problem, have different success rates. For example, the resistance distance and eigenvector centrality measures have been successful in revealing ecological pathways and differentiating between biomedical images of patients with Alzheimer's disease, respectively. The resistance distance measures an effective distance between two nodes of a network taking into account all possible shortest paths between them and the eigenvector centrality measures the relative importance of each node in a network. However, both measures require knowing the network's eigenvalues and eigenvectors. Here, we show that we can closely approximate [find exactly] the resistance distance [eigenvector centrality] of a network only using its eigenvalue spectra, where we illustrate this by experimenting on resistor circuits, real neural networks (weighted and unweighted), and paradigmatic network models — scale-free, random, and small-world networks. Our results are supported by analytical derivations, which are based on the eigenvector–eigenvalue identity. Since the identity is unrestricted to the resistance distance or eigenvector centrality measures, it can be applied to most problems requiring the calculation of eigenvectors.

Sign of a common pattern in social explosions

Mariano G. Beiró,^{1,2} Ning Ning Chung,³ Lock Yue Chew,^{4,5}
J. Stephen Lansing,^{6,7} Stefan Thurner,^{8,9} and Yérali Gandica¹⁰

¹*CONICET – Universidad de Buenos Aires. INTECIN, Argentina*

²*Universidad de Buenos Aires, Facultad de Ingeniería, Argentina*

³*Centre for University Core, Singapore University of Social Sciences, Singapore 599494.*

⁴*School of Physical & Mathematical Sciences, Nanyang Technological University, Singapore 637371.*

⁵*Data Science & Artificial Intelligence Research Centre, Nanyang Technological University, Singapore 639798.*

⁶*Santa Fe Institute, 1399 Hyde Park Road, Santa Fe, NM 87501, USA.*

⁷*Stockholm Resilience Centre, Kraftriket 2B, 10691 Stockholm, Sweden.*

⁸*Section for Science of Complex Systems, Medical University of Vienna, Spitalgasse 23, A-1090 Vienna, Austria.*

⁹*Complexity Science Hub Vienna, Josefstädterstraße 39, A-1080 Vienna, Austria.*

¹⁰*Laboratoire de Physique Théorique et Modélisation, UMR-8089 CNRS, CY Cergy Paris Université, France**

The success of an on-line movement could be defined in terms of the shift of scale and the later massive off-line protest. The role of the social media in this process is to facilitate the transformation between small or local feelings of disagreement into large-scale social actions. The way how social media achieves that effect is growing clusters of people and groups with similar effervescent feelings, which in other case would be never in communication by several constraints, as for instance, geographical distance.

Society is the emergent result from the interaction between their individuals. It is natural to think that any abrupt change in the structure, led by the communication between all the constituents, could be related to the percolating geometrical structures at the transition points. Independently of the kind of transition (in a physics sense), at the critical point the correlation length is expected to growth attaining a power-law dominance. The latter will, then, give rise to power-laws functionalities on the cluster's statistics forms.

In this respect, we propose that the transition online-offline protest is characterised by some signs of universality, as the expected consequences from the divergence on the correlation function at the critical point.

We show that the frequency-distribution of hashtags for several social explosions are power-law shaped. We have normalised our data-windows in terms of both the time and the number of hashtags. We defined as the transition point the day of the off-line massive actions in the streets.

The analysis has been performed on four different large-scale spontaneous manifestations. The first data set is the Spanish Indignados movement. The critical point for this data-set was the 15th of May 2011. The second and third data sets were taken in Argentina during the year 2019 around two popular movements: a protest against high taxes taking place between January 4th and 6th, and a mobilization asking for justice on November 9th. The last dataset is related to the “Occupy Wall Street” massive demonstrations taking place around May 2012.

Each data-set has been divided into the periods before, during and after the event. The period during the event is the most important, as it sets the time-scale. This is regularly of one day, except for the movement 9-N, which took place during two-days, and the Occupy Wall Street, which is a long-term event. Then, we divided our analysis into two parts, according to how we define the periods before and after the event: for the first analysis, we use the same amount of time to designate the other two periods, namely, before and after. In a second analysis, we extend the timeline before and after the event as to cover the same number of hashtag usages. In figure 1 we plot the number of hashtags used in each period, each segment having the same time-window. Blue, yellow and red designate the periods before, during and after, respectively. We can see completely different kinds of behaviors for the four movements. No similarities seem to appear beyond the highest activity during the event. As an illustration, in figure 2 we show the distributions for the frequency of hashtags on the the data set in figure 1 and the fit for the power-laws exponents.

Our results show that the lowest values for the exponents occur on the data-set ”during” for all the events. That consequence of the highest heterogeneity on the distribution is expected for the case of the same-time data-sets, then varying the number of hashtags. However, it starts to be interesting the fact that this is maintained also when the data is divided by having the same number of hashtags, then varying the time. Here there are not more hashtags in that window of time.

* ygandica@gmail.com

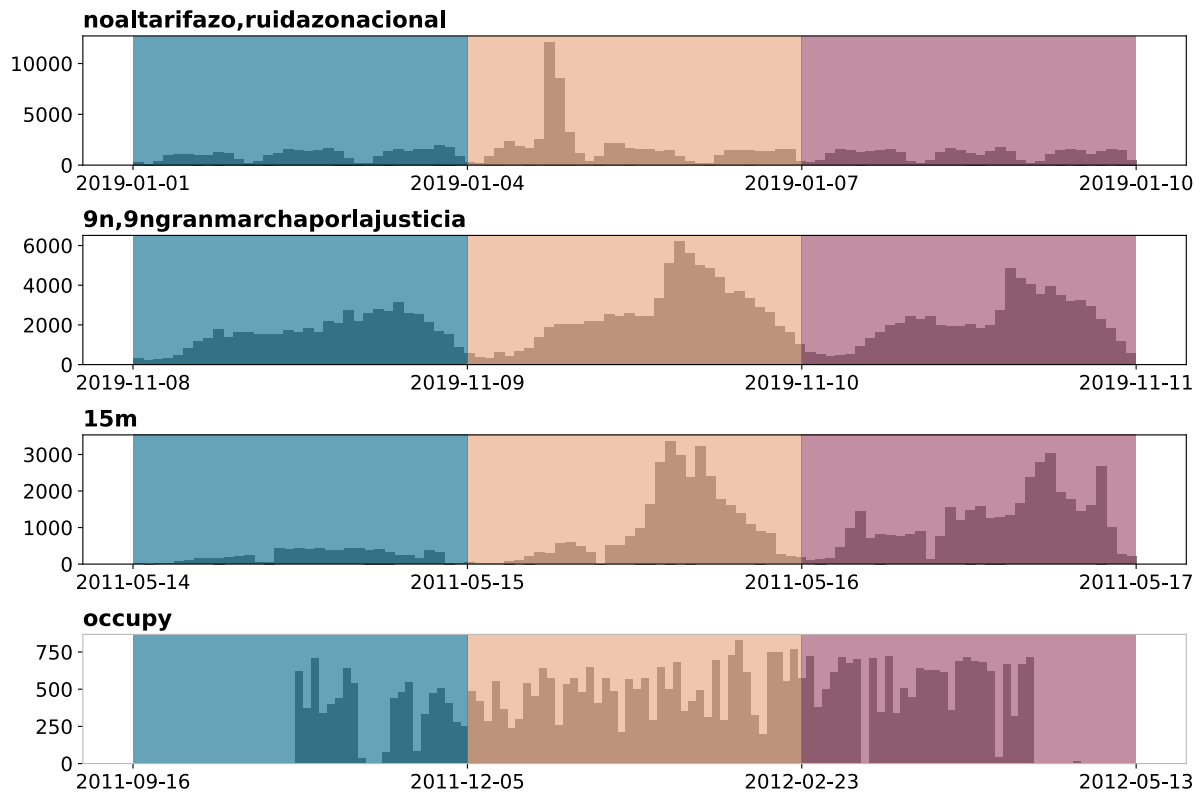


FIG. 1. Daily activity in each dataset in terms of number of tweets, classified as before, during, and after the online-street-action switch-event date. Each segment has the same time-window. No similarities were found on the four events beyond the higher activity on the period during.

One of the most interesting results is that the exponents of the periods "before" and "during" are the same, within the error bars. That happens when the periods have the same time windows but also when they have, instead, the same number of hashtags. The most surprising finding is that the last phenomena is robust against counting one or all the usages of the hashtags.

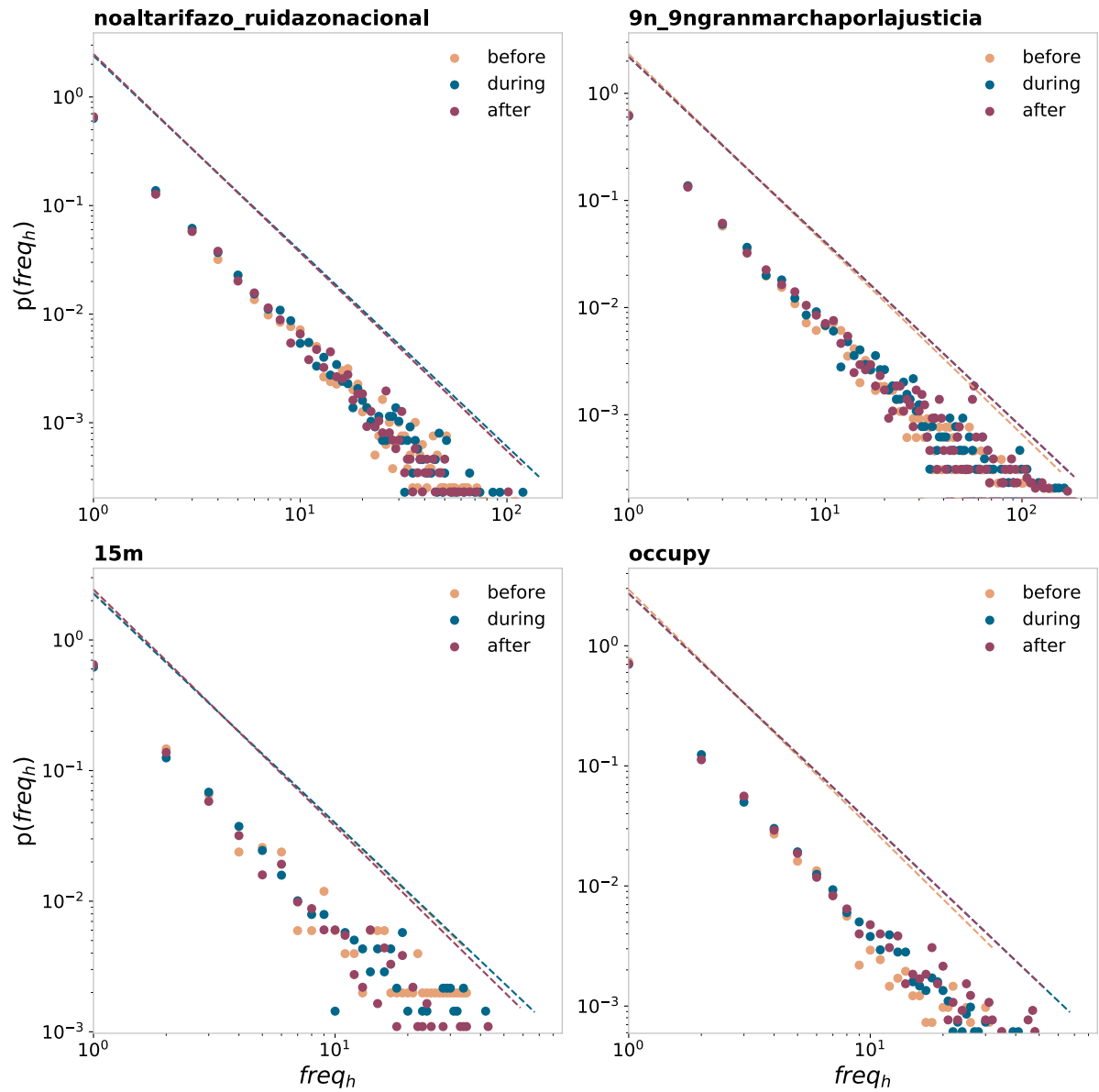


FIG. 2. Probability distributions of hashtag usage for each data-set, classified as before, during, and after the events (using a similar time extension for the 3 intervals), with their respective fitted exponents.

On the performance of a flow energy harvester using time delay

This paper explores periodic vibration-based energy harvesting (EH) in a delayed harvester device consisting of a delayed nonlinear oscillator subject to galloping excitation and coupled to an electric circuit through a piezoelectric coupling mechanism. It is assumed that the delay amplitude is modulated such that the frequency of the modulation is near twice the natural frequency of the oscillator. Application of the method of multiple scales gives approximation of the amplitude of periodic vibrations and the corresponding power extracted from the harvester device. Results show that the presence of modulated delay amplitude in the mechanical component increases significantly the amplitude of vibrations and the output power in a certain range of the wind speed. Numerical simulation is conducted to support the analytical predictions.

Markovian Anticipation in PERM simulations of high-dimensional SAWs: A study of guidance in rare-event simulations for non-Markovian systems

"Guidance" is a strategy to reduce fluctuations in rare event simulations. For Markov processes (including diffusion-type quantum Monte Carlo), ideal guidance can at least be defined, but for non-Markovian processes only heuristic proposals are available. One such heuristic is, in the framework of the PERM algorithm, "Markovian anticipation (MA)". We study in this paper MA systematically in self-avoiding walks on lattices with high coordination numbers. In particular, we present improved estimates of the connectivity constant for fcc and bcc lattices in 3 dimensions, and for all hypercubic lattices with $d=4$ to 10.

Observation of bifurcations and hysteresis in experimentally coupled logistic maps

Initially, the logistic map became popular as a simplified model for population growth. In spite of its apparent simplicity, as the population growth-rate is increased the map exhibits a broad range of dynamics, which include bifurcation cascades going from periodic to chaotic solutions. Moreover, the study of coupled maps allows to identify other qualitative changes in the collective dynamics, such as hysteresis. Particularly, hysteresis is the appearance of different attracting sets, one when the control parameter is increased and another one when it is decreased; that is, a multi-stable region. In this work, we present an experimental study on the bifurcations and hysteresis of nearly identical, coupled, logistic maps. Our logistic maps are an electronic system that has a discrete-time evolution with a high signal-to-noise ratio ($\sim 10^6$), resulting in easy, precise, and reliable experimental manipulations, which include the design of a modifiable diffusive coupling configuration circuit. We find that the characterisations of the isolated and coupled logistic-maps' dynamics agrees excellently with the theoretical and numerical predictions (such as the critical bifurcation points and Feigenbaum's bifurcation velocity). Here, we report multi-stable regions appearing robustly across configurations, even though our configurations had parameter mismatch, which we measure directly from the components of the circuit and also infer from the resultant dynamics for each map, and were unavoidably affected by electronic noise.

Entropy production fluctuation in phase transitions

The study of equilibrium systems is well established, however the vast majority of phenomena occurring in nature or in technological applications are out of equilibrium. Stochastic Thermodynamics is a framework developed to extend the knowledge of equilibrium to non-equilibrium systems, which comprises the study of phase transitions. During a first-order non-equilibrium phase transition, as in equilibrium ones, the system presents a distinguishing bistable behavior, which features the break of ergodicity. To assess the statistics of fluxes in out of equilibrium systems the most common tool, Large Deviation Theory [1], considers the long-time limit. However the bistable behavior can make this task quite tricky, the time it takes for the system to jump between one stable state to the other increases exponentially with the volume [2], hence it does not require much to make the so called long-time limit unfeasible. In this work we address the subtleties of assessing the statistics of fluxes during a discontinuous phase transition, in specific the entropy production, a key concept that quantifies how much the system is out of equilibrium and presents striking features at phase transitions [3]. Predictions are verified both analitically and numerically using the second Schlogl's model for chemical reactions [4] and a q-states Potts model. [1] Touchette, Hugo. *Physics Reports* 478.1-3 (2009): 1-69. [2] Nguyen, Basile, and Udo Seifert. *Physical Review E* 102.2 (2020): 022101. [3] Noa, CE Fernandez, Harunari, Pedro E, et al. *Physical Review E* 100.1 (2019): 012104. [4] Schlogl, Friedrich. *Zeitschrift fur physik* 253.2 (1972): 147-161

Generalized Hamiltonian mean-field models

Velimir Ilić^{1,*} and Shamik Gupta²

¹Mathematical Institute of the Serbian Academy of Sciences and Arts, Beograd, Serbia

²Ramakrishna Mission Vivekananda Educational and Research Institute, Belur Math, India

*Corresponding author (email: velimir.ilic@gmail.com)

Hamiltonian mean field (HMF) model is a prominent example of a long-range interacting (LRI) system, which was widely discussed in the past, and it predicts plenty of interesting phenomena, such as the appearance of the second order equilibrium phase transitions [Campa et al. 2009] and slow relaxation towards the equilibrium in non-equilibrium regime [Yamaguchi et al. 2004]. In this paper we propose a family of general transformations of the HMF model, by which we construct a family of generalized HMF models, which includes previously discussed HMF alternatives [Anteneodo 2004], [Toral 2004], [Ilić-Gupta 2021], [Velazquez et al. 2003], and we expose the qualitatively same critical phenomena at the microcanonical level with the quantitatively different equilibrium and non-equilibrium behaviors compared to the ordinary HMF model.

The transformations consist of Hamiltonian rescaling (H-rescaling) and rescaling of a conjugated variable (P-rescaling), which are coupled with the rescaling of the time variable to preserve Hamiltonian equations of motion. We established a relationship between the H-rescaling, the extensivity of energy and the value of the phase transition point in the generalized HMF model, which deviates from the critical value of the ordinary HMF model. On the other hand, the P-rescaling is related to the extensivity of entropy and its Gibbs factor [Yûto-Ueda 2007], as well as to the non-equilibrium behavior of the model, thus providing a new form of the famous "1.7-slow relaxation law" [Yamaguchi et al.], which opens up new possibilities for the characterization of LRI systems such as a fully coupled network of classical rotators [Antoni-Ruffo 1995].

REFERENCES

- [Campa et al. 2009] Campa, A., Dauxois, T., & Ruffo, S. (2009). Statistical mechanics and dynamics of solvable models with long-range interactions. *Physics Reports*, 480(3-6), 57-159.
- [Yamaguchi et al. 2004] Yamaguchi, Y. Y., Barré, J., Bouchet, F., Dauxois, T., & Ruffo, S. (2004). Stability criteria of the Vlasov equation and quasi-stationary states of the HMF model. *Physica A: Statistical Mechanics and its Applications*, 337(1-2), 36-66.
- [Anteneodo 2004] Anteneodo, C. (2004). Nonextensive scaling in a long-range Hamiltonian system. *Physica A: Statistical Mechanics and its Applications*, 342(1-2), 112-118.
- [Toral 2004] Toral, R. (2004). On the nonextensivity of the long range XY model. *Journal of statistical physics*, 114(5), 1393-1398.
- [Ilić-Gupta 2021] Ilić, V., Gupta, S. (2021). Extensive scaling and phase transitions in non-homogenous HMF model. *16th Joint European Thermodynamics Conference Prague*, June 14–18, 2021
- [Velazquez et al. 2003] Velazquez, L., Sospedra, R., Castro, J. C., & Guzman, F. (2003). On the dynamical anomalies in the Hamiltonian Mean Field model. *arXiv preprint cond-mat/0302456*.
- [Yûto-Ueda 2007] Murashita, Y., & Ueda, M. (2017). Gibbs paradox revisited from the fluctuation theorem with absolute irreversibility. *Physical review letters*, 118(6), 060601.
- [Antoni-Ruffo 1995]. Antoni, M., & Ruffo, S. (1995). Clustering and relaxation in Hamiltonian long-range dynamics. *Physical Review E*, 52(3), 2361.

Study of aging and failure using lifetime statistics of thin liquid films

Ali Irannezhad¹, Stefan Hutzler¹, Peter Richmond¹, and Bertrand M. Roehner²

¹School of Physics, Trinity College Dublin, Dublin, Ireland,

²Institute for Theoretical and High Energy Physics (LPTHE), Pierre and Marie Curie campus, Sorbonne University, Centre de la Recherche Scientifique (CNRS), Paris, France.

Recently it has been demonstrated that collections of thin liquid films, contained in cylinders, may be used as model systems for the study of failure or aging. The experiments showed that the mortality/failure rate of such films displays the characteristic bath-tub curve found not only for many technical devices, but also in the statistics of human mortality; an initially high failure rate ("infant mortality") decreases to a minimum, only to rise again with time (called wear-out phase for technical devices).

In this study, we focus on early-stage (infant) mortality for soap films as a simple well-controlled physical system. Using measurements of lifetimes for soap films, we show how mortality/failure rate links to geometry of the system; here, this is the length of the tube containing the films. This is required to further explore the use of such films as an easily experimentally accessible model system for aging studies.

[1] Haffner, B., Lalieu, J., Richmond, P., Hutzler, S.: Can soap films be used as models for mortality studies? *Physica A: Stat. Mech. Appl.* 508, 461–470 (2018).

[2] Bois, A., Garcia-Roger, E.M., Hong, E., Hutzler, S., Irannezhad, A., Mannioui, A., Richmond, P., Roehner, B.M., Tronche, S.: Physical models of infant mortality: implications for defects in biological systems. *Journal of Biological Physics* 46 (4), 371-394 (2020).

[3] Richmond, P., Roehner, B.M., Irannezhad, A., Hutzler, S.: Mortality: A physics perspective. *Physica A: Statistical Mechanics and its Applications*, 125660 (2020).

Epidemic Spreading and Digital Contact Tracing: Effects of Heterogeneous Mixing and Quarantine Failures

Abbas K. Rizi,¹ Ali Faqeeh,^{1,2,3} Arash Badie-Modiri,¹ and Mikko Kivelä¹

¹*Department of Computer Science, School of Science, Aalto University, FI-0007, Finland*

²*Mathematics Applications Consortium for Science & Industry, University of Limerick, Ireland*

³*CNetS, School of Informatics, Computing, & Engineering, Indiana University, Bloomington, IN, USA*

(Dated: July 6, 2021)

Contact tracing via digital tracking applications installed on mobile phones is an important tool for controlling epidemic spreading. Its effectivity can be quantified by modifying the standard methodology for analyzing percolation and connectivity of contact networks. We apply this framework for networks with varying degree distribution, the number of application users and the probability of quarantine failure. Further, we include structured populations with homophily and heterophily and the possibility of degree-targeted application distribution. Our results are based on a combination of explicit simulations and mean-field analysis. They indicate that there can be major differences in the epidemic size and epidemic probabilities which are equivalent in the normal SIR processes. Further, degree heterogeneity is seen to be especially important for the epidemic threshold but not as much for the epidemic size. The probability that tracing leads to quarantines is not as important as the application adoption rate. Finally, both strong homophily and especially heterophily with regards to application adoption can be detrimental. Overall, epidemics are very sensitive to all of the parameter values we tested out, which makes the problem of estimating the effect of digital contact tracing an inherently multidimensional problem.

In a pandemic era, until effective vaccines are widely deployed, carefully timed non-pharmaceutical interventions [1] such as wearing face masks [2], school closures, travel restrictions and contact tracing [3–7] are the best tools we have for curbing the pandemic. Contact tracing is an attempt to discover and isolate asymptomatic or pre-symptomatic (exposed) individuals. In the absence of herd immunity, contact tracing is a potent low-cost intervention method since it puts people into quarantine where and when the disease spreads. Therefore, it can have a major role in 1) containing a pandemic by relaxing social-distancing interventions [8], 2) providing an acceptable trade-off between public health and economic objectives [9, 10], 3) developing sustainable exit strategies [11, 12], 4) identifying future outbreaks [13] and 5) reaching the ‘source’ of infection [14].

Thanks to the emergence of low-cost wearable health devices [15–21] and mobile software applications, digital contact tracing can now be deployed with higher precision without the problems of manual contact tracing such as the tracing being slow and labor-intensive or having human issues related to blame, fear, confusion and politics. On the other hand, smartphone cameras and wearable devices also offer continuous access to real-time physiological data which can be used to tune other non-pharmaceutical or pharmaceutical strategies. Modern apps enable us to monitor COVID-19 symptoms [22–24] and identify its hotspots [25], track mosquito-borne disease such as Malaria, Zika and Dengue [26, 27] and detect microscopic pathogens.

In both forms — manual [4, 5, 28–36] and digital [37–40] — contact tracing has been commonly considered as an effective strategy and different empirical data sets have validated this claim in short-time population-based controlled experiments [37, 41–45]. It has been estimated

that for every percentage point increase in app users, the number of cases can be reduced 2.3% (statistical analysis) [46]. Its real potential in heterogeneous [47–50] populations, however, is not yet clear, especially because of the homophily in app adoption and other health behaviors [51, 52]. It has been reported that app adoption is correlated with people’s job, age, income and nationality [53, 54]. Degree-heterogeneity in the contact network [55] can alter epidemiological properties in the form of variance in final outbreak size [56], vanishing epidemic threshold [50, 57], hierarchical spreading [58], strong finite-size effects [59] and universality classes for critical exponents [60].

To reduce the peak and total size of the epidemic, not only the number of app adoption but also its distribution is of great significance if contact tracing is done early enough in the course of the spread. Therefore, in some parameter settings, contact tracing may not be effective enough [8, 61, 62]. To curb the epidemic, app adoption of super-spreaders [63, 64] are needed to be taken into account since it dictates the extent to which a virus spreads in a bursty, power-law fashion [65–67] especially when there is high individual-level variation in the number of secondary transmissions [58, 68, 69].

Since the World Health Organization has declared the COVID-19 outbreak as a Public Health Emergency of International Concern, network scientists have developed different approaches towards analyzing epidemic tracing and mitigation with apps. Using the toolbox of network science, different groups have investigated the effectiveness of contact tracing based on the topology and directionality of contact networks [14, 41, 70–76]. Recently, a mathematical framework aimed at understanding how homophily in health behavior shapes the dynamics of epidemics has been introduced by Burgio *et al.* [77].

In this study, we investigate the effect of varying app coverage in homogeneous and heterogeneous contact networks with and without homophily in app adoption. Further, we explore the effect of distributing the apps randomly and preferentially to high-degree nodes [70] in these scenarios. Our main focus is on the epidemic threshold and the final size of the epidemics, therefore, we assume the dynamics of the epidemic to be governed by the simple SIR model [55]. This model can be easily mapped to a static bond-percolation problem [78, 79] so that the epidemiological properties can be measured based on the topological structure of the underlying network [55, 80–83]. The difference in the spreading framework with the app to the normal one is that the infection cannot spread further if it passes a link between two app-users (app-adopters). That is, the infection process model needs to include the memory of the type of node it is coming from. We then extend the percolation framework such that we can add memory [84, 85] to it in order to keep track of the infection path. This leads to the observation that the epidemic size is not the same as the epidemic probability anymore.

Our results are largely based on mean-field-type calculations of the percolation problem which are confirmed by explicit simulations of SIR epidemic process and measurements of component sizes in finite networks. Our findings show that 1) number of app-users has a direct effect on the epidemic size and epidemic probability and the difference between these two observables is larger in high-degree targeting strategy, 2) epidemics can be controlled to much better in the high-degree targeting strategy, 3) even though degree-heterogeneity can strongly affect or even vanish the epidemic threshold, high-degree targeting strategy can compensate this effect and increase the threshold significantly, 4) increasing heterophily from random mixing always increases the outbreak size and lowers the epidemic threshold, 5) increasing homophily does the opposite until an optimum, that is below the maximum homophily case, is reached and 6) the probability of contact tracing succeeding in preventing further infections is not as important as the fraction of app-users, but can still have significant effects on the epidemic size and epidemic threshold. The only exception is in the case of heterogeneous networks with high-degree targeting strategy, since hubs play a significant role there.

I. MODELLING APPROACH

A. Disease model and connection to percolation

We employ a standard SIR disease model on networks with additional dynamics given by the disease interactions with the disease tracking application. In the model, an infected (I) node will infect susceptible (S) nodes it is connected to by rate β and go to the removed state (R) after time τ .

In addition, if an app-user infects another app-user, that second node will get infected but will quarantine themselves with probability p_{app} . The quarantined user will have no further connections that would spread the infection they received from the other app-user. A noteworthy deviation from a realistic spreading case here is that we do not model quarantines that would be caused by another app-user but prevent the disease spreading through a third node. That is, we only model the primary infection path from the other app-user causing the alarm, but do not stop possible concurrent secondary infection paths from a third node.

The SIR processes can be studied using component size distributions of networks where parts of the links are randomly removed. In the presence of apps, the SIR spreading process can be mapped to a slightly more complicated percolation problem [41, 70]. Thus, the epidemic threshold, epidemic probability and epidemic size can be read from percolation simulations [78, 86, 87]. In this mapping, every infected individual, regardless of app adoption, can infect a susceptible neighbor with transmission probability $p = 1 - e^{-\beta\tau}$ [78]. Moreover, to model the quarantines by app-users one needs to delete the links between two app-users with probability p_{app} . This ensures that we ignore the infection paths that would go through two app-users when one of them is successfully quarantined. However, removing these links also removes the second app-user from the component, even though they are infected. To correct for this we need to first find the components of the network, and then extend them, by including all app-users outside of the component that are connected to another app-user (and considering the probability p that the link is kept). See Fig. 1 for an illustration of this process, which leads us to two definitions of components: normal and extended.

B. Components, epidemic size and epidemic probability

In the SIR model without apps, the component size distribution can be used to fully describe the late stages of the epidemics. Given an initially infected node, the size of the component it belongs to determines the size of the epidemic. The relationship between percolation and the final disease size is particularly simple if the population is large enough that it can be approximated with an infinite contact network. In this case, the percolation threshold gives the epidemic threshold and below it the epidemic always spans only a zero fraction of the population, because all the components are of finite size. Above the percolation threshold there is a single giant component which spans $s_{\text{max}} = S_{\text{max}}/N$ fraction of the nodes. This is equivalent to both the size of the epidemic, given that there is one, and the probability that there is an epidemic starting from a single initially infected node [78]. The expected size of the epidemics is in this case given as S_{max}^2 .

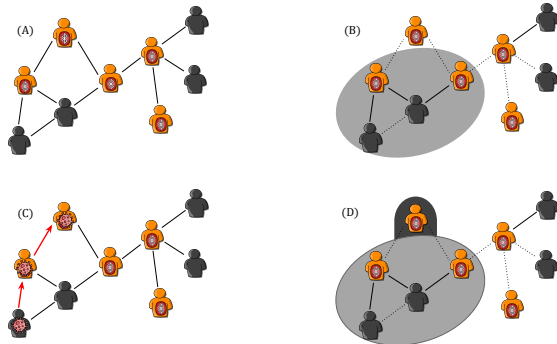


FIG. 1. (a) Original contact network with app-users marked with the oval symbol. (b) The normal largest component, after the dotted links have been removed in the percolation process by random. When apps are working perfectly, links between a pair of app-users are removed with probability $p_{\text{app}} = 1$ and other links are removed with probability p . (c) An example for a path of infection: the second app-user can be infected therefore it must be included in the outbreak size (d) Extending the giant component to include the secondary app infections. The second infected app-adaptor is added to the giant component with transmission probability p .

When we introduce apps to the spreading process the equivalence of the epidemic size and epidemic probability breaks down. Both the normal component and the extended component become important. The probability that there is an epidemic is still given by the component size as in the normal SIR process. However, the epidemic size, given that there is one, is now given by the extended component size S'_{max} . The expected epidemic size is then given by $S_{\text{max}} S'_{\text{max}}$.

Similar relationships hold for finite-size systems. For example, the expected size of the epidemics from single source becomes

$$\langle E \rangle = \sum_c \frac{S_c}{N} S'_c, \quad (1)$$

where S_c is the normal size and S'_c is the extended size of the component c and N is the total number of nodes. In this formula, S_c/N gives the probability that the initially infected node is in the component c and S'_c gives the size of the epidemic if a node in component c is chosen.

C. Network models

We aim to study how the network topology and the locations of the app-users in the network affect the epidemics. We study networks with degree distribution $P(k)$ and average degree $\langle k \rangle$ such that each node is an app-user with probability π_a and not an app-user with probability $1 - \pi_a$. We use Poisson (ER) random graphs [88] to model homogeneous contact patterns and scale-free networks generated with the configuration model [55]

where $P(k) \propto k^{-3}$ to model heterogeneous contact patterns. The $\pi_a N$ app-users can be picked 1) uniformly at random from the underlying network or 2) by distributing the apps in the order of their degree such that the high-degree nodes get the apps first.

To insert homophily (heterophily) in app adoption, we assume that app-users are more likely (are less likely) to be connected together. This can be controlled by the probability π_{aa} that an app-user is connected to another app-user; this stochastic block model network is a type of $E^{i,i'}$ network introduced in Ref [89] with two groups of nodes: app-users and individuals without the app. The existence of homophily or heterophily of the network structure is determined by comparing π_{aa} to its value for the neutral case with no homophily or heterophily.

In the absence of homophily or heterophily, $\pi_{aa} = \eta_a$, where η_a is the ratio of links that emerge from app-users to the total number of stubs (nodes connections); this is because if the nodes were connected purely at random, the probability that a link from an app-user connects it to another app-user equals the ratio of the number of stubs that app-users have to the total number of stubs, i.e., η_a . In the case of a random selection of app-users $\eta_a = \pi_a$, since both app-users and non-app-users have on average the same number of stubs and the fraction of stubs that app-users have equals the fraction of app-users in the system, i.e., π_a . Nonetheless, in a high-degree targeting strategy, the number of stubs that app-users have on average is larger than that of non-app-users. In that case, η_a can be calculated from the degree distribution (see Sec. II A). When $\pi_{aa} > \eta_a$, app-users are more likely to be connected to each other than a purely random network in which they are connected with probability η_a . Hence in that case there is homophily in the connection between the app-users, which means there is also homophily in the connections between non-app-users. On the other hand, when $\pi_{aa} < \eta_a$ nodes are more likely to be connected to the nodes of the other type (heterophilic network).

II. ANALYTIC AND SIMULATION METHODS

The epidemics are here studied with various methods of approximation. We employ analytical computations based on mean-field-type approximations to efficiently analyse the wide parameter space of our models and to provide explicit formulas for our main observable quantities. Here an approximation based on branching processes can be used to determine the critical point. Following Ref. [41], more detailed calculation based on percolation arguments will give us the component sizes which can be related to the final epidemic size and epidemic probability. These mean-field approximations are then complemented by simulations of the network connectivity. Finally, we explore the accuracy of the mean-field approximations via explicit simulations of the SIR model.

A. Giant component size from consistency equations

To study the behavior of the epidemic dynamics we form consistency equations for the giant component size. In Ref. [41] the governing equations for the size of the epidemic and the transition point were obtained for the case of random networks in the absence of homophily. Here we derive the analytical results for the more general case of the spectrum of heterophilic to homophilic networks, a special case of which are the non-homophilic networks of Ref. [41]. We consider that app-users might be connected together with a pattern different from pure random chance, this can also be the case for the non-users. In the case of a homophilic network where the app-users are more likely to be connected together, the non-users are also more likely to be connected to individuals of the same kind. This is equivalent to saying that groups of people who adopted the app are likely to be groups of nodes in the network with members in rather close distance from each other. To represent the bias in connection probabilities we consider that a link from an app-user is connected to another app-user with probability π_{aa} and other types of links were formed with probabilities $\pi_{an} = 1 - \pi_{aa}$, $\pi_{na} = \frac{\pi_a}{1 - \pi_{aa}}(1 - \pi_{aa})$ and $\pi_{nn} = 1 - \pi_{na} = \frac{1 - \pi_a - \pi_a(1 - \pi_{aa})}{1 - \pi_{aa}}$, where π_a is the probability that a person is an app-user and the second equality comes from the balance between the number of links from app-users to non-app-users and from non-app to app-users, that is, $\pi_a N \pi_{an} \langle k \rangle = (1 - \pi_a) N \pi_{na} \langle k \rangle$.

Our aim is to write the self-consistency equations for the probability, u_0 , that following a link to a non-app-user does not lead to the giant component and probability u_a , that following a link to an app-user does not lead to the giant component. Using these probabilities the relative size of the giant component s and the relative size of the extended giant component s' can be obtained, where s is in fact the fraction of nodes infected through non-app-users, while s' also includes individuals caught infection though an app-user before s/he could quarantine her/himself (see Sec. II C 1).

Similar to Ref. [41], we can write the conditional probabilities of u_0 and u_a given that they have degree k as

$$u_0(k) = \sum_{k'=0}^k \binom{k}{k'} \pi_{na}^{k'} u_a^{k'} (1 - \pi_{na})^{k-k'} u_0^{k-k'}, \quad (2)$$

$$u_a(k) = \sum_{k'=0}^k \binom{k}{k'} \pi_{aa}^{k'} (1 - \pi_{aa})^{k-k'} u_0^{k-k'}. \quad (3)$$

Then using a treatment similar to Ref. [41], the self-consistency equations can be written as:

$$u_0 = g_1((1 - \pi_{na})u_0 + \pi_{na}u_a), \quad (4)$$

$$u_a = g_1((1 - \pi_{aa})u_0 + \pi_{aa}(p_{app} + (1 - p_{app})u_a)), \quad (5)$$

and

$$s = 1 - (1 - \pi_a)g_0((1 - \pi_{na})u_0 + \pi_{na}u_a) - \pi_a g_0((1 - \pi_{aa})u_0 + \pi_{aa}(p_{app} + (1 - p_{app})u_a)), \quad (6)$$

where g_0 and g_1 are, respectively, the generating functions for degree and extended degree distributions [55], p_{app} is the probability the apps work as expected ($1 - p_{app}$ is then the probability that the app-user does not quarantine her/himself after being notified of exposure to an infectious app-user). Note that π_{na} is determined by the free parameters π_a and π_{aa} as we already showed that $\pi_{na} = \frac{\pi_a}{1 - \pi_{aa}}(1 - \pi_{aa})$.

We can approximate s' by writing:

$$s' = 1 - (1 - \pi_a)g_0((1 - \pi_{na})u_0 + \pi_{na}u_a) - \pi_a g_0((1 - \pi_{aa})u_0 + \pi_{aa}u_a), \quad (7)$$

where, as opposed to Eq. 6, the third term is not a function of p_{app} and the reason is that Eq. 6 assumes that if the app works (which happens with probability p_{app}) then the probability that a link connected to the app node does not lead to the giant component is 1 (while if the app doesn't work it is u_a). However, whether the app works or not, the probability that an app user does not get infected from another app user is u_a (the difference between the two cases is only that when the app works if the second app user is infected s/he quarantines her/himself and s/he doesn't infect any other node).

In the case of including a transmission probability p which is less than 1 (in the above equations it was assumed the links are transmitting with probability 1), Eqs. 4 and 5 will change to:

$$u_0 = 1 - p + pg_1((1 - \pi_{na})u_0 + \pi_{na}u_a), \quad (8)$$

$$u_a = 1 - p + pg_1((1 - \pi_{aa})u_0 + \pi_{aa}(p_{app} + (1 - p_{app})u_a)). \quad (9)$$

When the fraction π_a of nodes selected to adopt the app are all the highest degree nodes in the network, these nodes all have a degree higher than $k_a - 1$ such that they include some of k_a nodes and the rest are comprised of all nodes with degree larger than k_a . Then for the fraction η_a of the links protruding from the app-users (which are the top π_a fraction of nodes) can write:

$$\eta_a = r^* k_a p_{k_a} / \langle k \rangle + \sum_{k_a+1}^{\infty} k p_k / \langle k \rangle \quad (10)$$

$$= \sum_{k_{a,\text{right}}}^{\infty} k p_k / \langle k \rangle, \quad (11)$$

where r^* is the fraction of degree k_a nodes that are app-users and in Eq. 11 we absorbed r^* into p_k so that $p_{k_{a,\text{right}}} = r^* p_{k_a}$ represents the fraction of nodes in the network that have degree k_a and are app-users (so in Eq. 11, $k_{a,\text{right}}$ takes the value k_a).

Then for a network with homo/heterophily:

$$u_0 = 1 - p + p \frac{1}{1 - \eta_a} \sum_{k=0}^{k_{a,\text{left}}} q_k [(1 - \pi_{na})u_0 + \pi_{na}u_a]^k, \quad (12)$$

$$u_a = 1 - p + p \frac{1}{\eta_a} \sum_{k_{a,\text{right}}}^{\infty} q_k [(1 - \pi_{aa})u_0 + \pi_{aa}(p_{\text{app}} + (1 - p_{\text{app}})u_a)]^k, \quad (13)$$

and

$$s = 1 - \sum_{k=0}^{k_{a,\text{left}}} p_k [(1 - \pi_{na})u_0 + \pi_{na}u_a]^k - \sum_{k_{a,\text{right}}}^{\infty} p_k [(1 - \pi_{aa})u_0 + \pi_{aa}(p_{\text{app}} + (1 - p_{\text{app}})u_a)]^k. \quad (14)$$

A special case of which are networks with neutral (non-existing) homophily, where π_{aa} is obtained to be equal to η_a and accordingly $\pi_{na} = \eta_a$, therefore,

$$u_0 = 1 - p + p \frac{1}{1 - \eta_a} \sum_{k=0}^{k_{a,\text{left}}} q_k [(1 - \eta_a)u_0 + \eta_a u_a]^k \quad (15)$$

$$u_a = 1 - p + p \frac{1}{\eta_a} \sum_{k_{a,\text{right}}}^{\infty} q_k [\eta_a(p_{\text{app}} + (1 - p_{\text{app}})u_a) + (1 - \eta_a)u_0]^k, \quad (16)$$

and

$$s = 1 - \sum_{k=0}^{k_{a,\text{left}}} p_k [(1 - \eta_a)u_0 + \eta_a u_a]^k - \sum_{k_{a,\text{right}}}^{\infty} p_k [\eta_a(p_{\text{app}} + (1 - p_{\text{app}})u_a) + (1 - \eta_a)u_0]^k. \quad (17)$$

These results predict the behavior of the epidemic dynamics in the thermodynamic limit, therefore they describe the dynamics very well when the network size is large enough.

B. Mean-field approximation for the branching process

An alternative to writing the consistency equations for the giant component size is to assume that the epidemic dynamics is governed by a branching process. Then, an straightforward way of finding the epidemic threshold in the SIR model is to find the critical point of a branching process, where the branching factor is given by the expected excess degree q . In the epidemic setting the branching factor $\bar{k} = pq$ which gives the expected number

of people one infected person infects during the epidemic process. Note that this is different from the basic reproduction number that has been defined in the networks as $R_0 = \beta/\gamma\langle k \rangle$ [79]. In the SIR model with the app, we need to duplicate the populations so that we track separately the ones without the app (S_n, I_n and R_n) and with the app (S_a, I_a and R_a).

Given that the apps are uniformly distributed to π_a fraction of the nodes and \bar{k} is the branching factor, we can write a mean-field approximation based on the branching process as follows:

$$I_n^{(t+1)} = \bar{k} (\pi_{nn} I_n^{(t)} + \pi_{an} I_a^{(t)}), \quad (18)$$

$$I_a^{(t+1)} = \bar{k} (\pi_{na} I_n^{(t)} + \pi_{aa} (1 - p_{\text{app}}) I_a^{(t)}). \quad (19)$$

By defining $a = \pi_{nn}\bar{k}$, $b = \pi_{na}\bar{k}$, $c = \pi_{an}\bar{k}$ and $d = \pi_{aa}\bar{k}(1 - p_{\text{app}})$, the difference equations can be written as:

$$\mathbf{X}_{t+1} = \mathbf{A}\mathbf{X}_t, \quad (20)$$

where $\mathbf{X}_t = \begin{pmatrix} I_n^{(t)} \\ I_a^{(t)} \end{pmatrix}$ and $\mathbf{A} = \begin{pmatrix} a & b \\ c & d \end{pmatrix}$.

The steady state $\mathbf{X}_{t+1} = \mathbf{X}_t$ is possible if all the eigenvalues λ of the transition matrix \mathbf{A} (whether real or complex) have an absolute value which is less than 1;

$$\lambda_{\pm} = \frac{a+d}{2} \pm \sqrt{\left(\frac{a+d}{2}\right)^2 - (ad-bc)}. \quad (21)$$

Without contact tracing, there is a chance of epidemic given the initial reproductive number is $\bar{k} > 1$. In the case of app adoption, the critical value of app-users π_a^c that are needed for reducing the reproductive number can be derived by setting $\lambda = 1$ which leads to:

$$\frac{1 - \pi_a(2 - \pi_{aa})}{1 - \pi_a} \left(\bar{k} + \bar{k}^2 \pi_{aa} (1 - p_{\text{app}}) \right) + \bar{k} \pi_{aa} (1 - p_{\text{app}}) + \frac{\bar{k}^2 \pi_a (1 - \pi_{aa})^2}{1 - \pi_a} = 1. \quad (22)$$

When apps work perfectly, the epidemic threshold is given by:

$$\bar{k}^c = \frac{\sqrt{1 + \pi_a \pi_{aa} [4(\pi_a + \pi_{aa}) - 3(\pi_a \pi_{aa} + 2)]}}{2\pi_a (\pi_{aa} - 1)^2} + \frac{2\pi_a - \pi_a \pi_{aa} - 1}{2\pi_a (\pi_{aa} - 1)^2}. \quad (23)$$

For each value of π_a there is a non-trivial optimum value π_{aa}^{opt} that leads to largest epidemic threshold in terms of the branching factor, which is:

$$\pi_{aa}^{\text{opt}} = \frac{\pi_a - 2}{3\pi_a - 4}. \quad (24)$$

The critical app adoption can be also calculated as:

$$\pi_a^c = \frac{1 - \bar{k}}{\bar{k}^2(\pi_{aa} - 1)^2 + \bar{k}(\pi_{aa} - 2) + 1}. \quad (25)$$

In the absence of homo/heterophily, $\pi_{aa} = \pi_a$, Eq. 22, gives the same result as of Ref. [41], such that:

$$\pi_a^c = \frac{\bar{k} - 1 + \sqrt{(\bar{k} - 1)(\bar{k} + 3)}}{2\bar{k}}. \quad (26)$$

C. Component size simulations

Next, we describe the way to extract the giant component in simulated networks and how these simulation results can be used for finding the critical points of the disease spreading process. The component sizes can also be used to find the epidemic size distributions as described in Section IB.

1. Component Extension

In each simulation run, we simulate one network structure G and distribute the apps to the nodes according to one of the models described in Section IC. From the original network G , we keep each link with probability $p = 1 - e^{-\beta\tau}$, which is the probability of infection going through a link without apps. We also remove all the links between two app-users with probability p_{app} and call the resulting network G_a . The components of graph G_a are the normal components.

The extended components can be reached by going through every normal component and extending it. For every app-user in the component $\alpha \in C$, we go through the neighbors $n_\alpha = \{\alpha_1, \alpha_2, \dots, \alpha_k\}$ in the original network G . If α_i is an app-user and not in the component $\alpha_i \notin C$, we add it to the component extension C' with probability p . The total set of infected nodes, if starting from a node in C , is going to be $C \cup C'$. As these are disjoint sets, we can compute the size as $S'_C = |C| + |C'|$ and $S_C = |C|$.

2. Susceptibility

In numerical simulations of finite size systems we can use the peak of a susceptibility measure to find the critical transition point. Theoretically, susceptibility [55] is a measure of fluctuation in the component sizes which is singular at the epidemic threshold (the critical point). In network percolation studies, it is defined as the expected growth in the size of the giant component when a random link is added to the network. Therefore, susceptibility in an ordinary percolation problem can be written as:

$$\chi = \frac{\sum_{c \neq c_{\max}} S_c^2 - S_{c_{\max}}^2}{N - S_{c_{\max}}}, \quad (27)$$

where S_c is the size of the component c , $c_{\max} = \text{argmax}_c S_c$ is the largest component.

This formulation of susceptibility is not suitable in the current case. In fact, using the maximum value of Eq. 27 could lead to estimates of critical points that are very far from the actual one. Instead, we want to compute the expected growth in the extended giant component, which can be computed as:

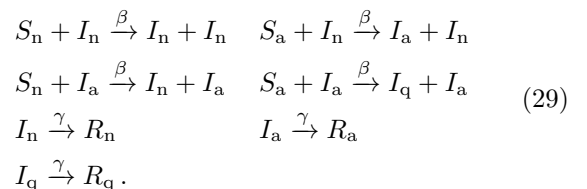
$$\chi' = \frac{\sum_{c \neq c_{\max}} S_c S'_c (1 - \frac{S'_{c_{\max}}}{N})}{N - S_{c_{\max}}}, \quad (28)$$

where S_c and S'_c are the size and the extended size of the component c and $c_{\max} = \text{argmax}_c S'_c$ is the largest component measured in the extended size.

D. Explicit compartment model simulations

Finally, we will perform explicit simulations of the spreading processes to confirm the theoretical results we arrived at via the approximations we presented above. The effect of tracking applications can be integrated into compartment model simulation by introducing separate susceptible and infected compartments for people with and without app. The interactions between people with no app installed is the same as normal SIR process, namely, susceptible individuals with no app S_n can become infected I_n by being in contact with infected people that either don't have the app installed I_n or have it installed I_a . However, if a susceptible individual with the app S_a comes into contact with an infected individual with app I_a , they will become infected but they will also receive infection notification from the app which means they will be quarantined I_q . Quarantined individuals cannot infect anyone else. Eventually, all the infected individuals will move to recovered compartment after a certain predetermined amount of time has passed. The recovered compartment is divided into three compartment (R_n , R_a , and R_q) to track from which infected compartment the node is originating from.

The set of all reactions can be written as follows:



Note that unlike most common SIR models, while edge reactions governed by Poisson processes happening at a constant rate β , node reactions are governed by constant cutoff time $1/\gamma$ and happen exactly $1/\gamma$ units of time after change in state.

As interactions in the simulation are bound to take place over edges of a static network, with nodes belonging to each of the compartments, as shown in Sec. III, the results are similar to a component size simulation (which

are described in Sec. II C) on a network with an effective connectivity of $\bar{k} = \langle k \rangle (1 - e^{-\beta/\gamma})$. As it is only the ratio between β and γ that plays as a parameter in the model, from now on we set the value of γ to 1.

In each simulation, starting from a single infected node and running the simulation in discrete time steps of 10^{-4} units until no further reaction is possible, the final number of nodes that end up in R_q , R_a and R_n determine total size of infection corresponding to the extended component size S' of the component that the initial seed node belongs to. Final combined size of the R_n and R_a component, however, represents the size of the component S_n that the seed node belongs to, had we removed app-app links. By adding I_a and I_q compartments, as compared to normal SIR processes, and linking them to the state of the source of infection and the internal state of each node, we are including information about history of the spreading agent more than one step back in simulation of the spreading process.

III. NUMERICAL RESULTS

We will next illustrate using the theory and simulation introduced in Sec. II how the various parameters affect the epidemic sizes and epidemic probabilities. The simulation studies are done in networks of 10^4 nodes and averaged over 10 realizations. We use two network topologies: homogeneous networks (Erdős-Rényi networks) with expected degree $\langle k \rangle = 10$ and networks created with the configuration model with power-law degree distribution $p(k) \propto k^{-3}$, where the amount of degree 1 nodes is adjusted such that the average degree is 10.

A. Differences in normal and extended components

The difference of the epidemic probability (normal component size) and the epidemic size (extended component size), is a phenomenon that is specific to epidemics in the presence of app-adaptors. Breaking the equivalence of these two measures can have practical consequences as illustrated in Fig. 2a. The difference between these two grows with the fraction of app-users π_a . For example, when $\pi_a = 0.8$ and the epidemic probability (the normal component size) is $s_{\max} \approx 0.5$, the epidemic size (the extended component size) reaches $s_{\max} \approx 0.8$. This is reflected also in the expected epidemic sizes (see Fig. 2b). Despite the two component definitions differing from each other, they still display the transition at the same point and this point can be measured numerically using the susceptibilities defined in Eqs. (27)-(28) (see Fig. 2c).

The extended component size is not a conserved quantity like the normal component size in the sense that the sum of component sizes S_{Σ} would always sum to the number of nodes N . Instead, the sum of component sizes can be significantly larger than the number of nodes (see

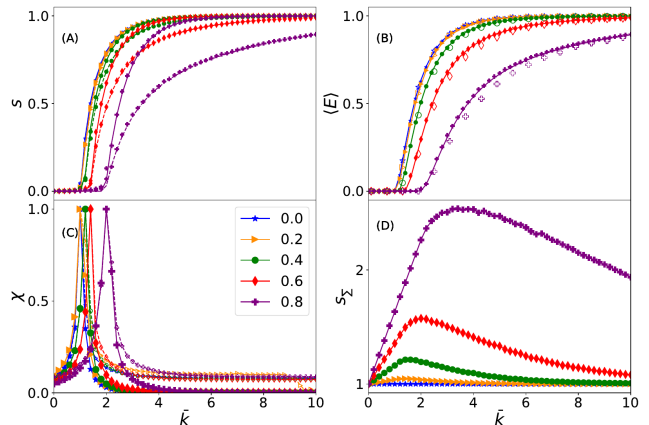


FIG. 2. Disease spreading statistics in an Erdős-Rényi network as a function of the effective degree \bar{k} when there are π_a applications that are distributed uniformly randomly. Results are normalised to the network size N and shown for $\pi_a \in [0, 0.2, 0.4, 0.6, 0.8]$ with different markers. (a) The normal component size, i.e., the epidemic probability, (dashed lines and markers following them) and the extended components, i.e. the epidemic size, (solid lines and markers following them). Dashed and solid lines indicate the results from theory introduced in Sec. II A and the markers are results computed from component sizes of simulated networks as described in Sec. II C. (b) The expected epidemic size computed with theoretical results introduced in Sec. II A (solid lines), simulated component sizes introduced in Sec. II C (filled markers), and explicit SIR simulations introduced in Sec. II C (empty markers). (c) Susceptibility of the normal giant component χ (dots) and the extended component χ' (solid lines). Peaks are at the same positions for both types of curves. (d) The fraction of sum of component sizes and network size S_{Σ}/N .

Fig. 2d) and the maximum value it can reach grows with the number of application users π_a . The deviation from $S_{\Sigma}/N = 1$ reaches its maximum with disease parameters higher than the threshold values, but when the disease reaches a large enough population the fraction S_{Σ}/N starts to decay reaching $S_{\Sigma}/N = 1$ when everybody belongs to the normal giant component.

B. Quarantine failures

The assumption in Section III A is that i) apps work perfectly and ii) an app-user always self-isolates before having a chance to apps the infection, meaning that there are no quarantine failures, $p_{\text{app}} = 1$. It is of practical significance to investigate the effects of quarantine failures [46] on the epidemic threshold and epidemic size. Fig. 3 shows that in the absence of major quarantine failures, epidemic tracing and mitigation with apps can still be a valid strategy if app adoption level in a society is high enough. The effect of app adoption rate π_a is more important than the rate at which apps function, but both need to be relatively high in order for the apps to have a significant impact.

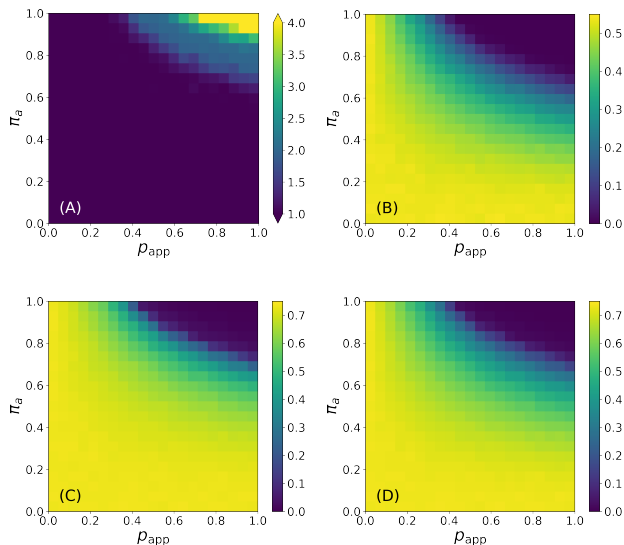


FIG. 3. The effect of quarantine failures in homogeneous networks when app adoption is done uniformly randomly. (a) The epidemic threshold as a function of quarantine probability p_{app} and app adoption rate π_a . All threshold values larger than 4 are shown with the same color. By setting the effective connectivity of the network to $\bar{k} = 1.8$ (b) the expected epidemic size, (c) the extended giant component size and (d) the normal giant component size are shown as a function of p_{app} and π_a .

Even if we are above the epidemic threshold, the apps can be useful. Especially when the application adoption π_a is high, the quarantines can be very unreliable and the outbreak size (Fig. 3b-c) and epidemic probability (Fig. 3d) both remain small. Again, overall both the app adoption and quarantine reliability are important, with the app adoption rate being more important.

C. Degree heterogeneity and high-degree app targeting

Real networks are degree-heterogeneous and this heterogeneity has a strong effect on the final outbreak size and the epidemic threshold. Fig. 4 shows the expected epidemic sizes with two different strategies in app adoption, random and high-degree targeting for different fractions of app-users π_a in the network. In homogeneous networks, Fig. 4a, contact tracing decreases the expected epidemic size and pushes the epidemic threshold forward. These effects can be further amplified by shifting to the high-degree targeting in app adoption. With 80% of app-users, the epidemic threshold can move from $\bar{k} = 1$ to $\bar{k} = 4$ which means at that point expected epidemic size is zero while without contact tracing it would be almost 1. Note that in homogeneous networks, the effective average degree of the contact network \bar{k} , has a good correspondence to the reproduction number of the infection.

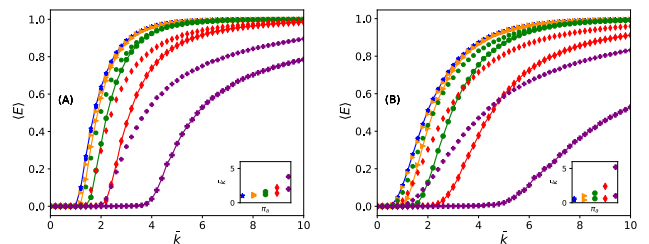


FIG. 4. Expected epidemic size $\langle E \rangle$ as a function of effective degree \bar{k} . Results are shown for different values of π_a using different markers: 0 (stars), 0.2 (triangles), 0.4 (discs), 0.6 (diamonds), and 0.8 (crosses). The solid lines with markers indicate the high-degree targeting strategy while single markers indicate the random app adoption. The insets show the epidemic threshold for the two strategies as a function of app-adoption rate π_a (such that the upper point is always the high-degree targeting strategy). Results are shown for two network topologies; (a) homogeneous networks with Poisson degree distribution and (b) heterogeneous networks with a power-law degree distribution $P(k) \propto k^{-3}$.

In networks with degree-heterogeneity, the epidemic threshold vanishes in normal SIR processes. This effect holds in contact-traced epidemics if we distribute the apps uniformly randomly. However, from Fig. 4b it is clear that contact tracing can significantly reduce the expected epidemic size even when the apps are randomly distributed and the epidemic threshold remains unchanged. With a high-degree targeting strategy, it is possible to move the epidemic threshold. Comparing the expected epidemic size at different values of $\bar{k} < 3$ shows that in real-world situations, app adoption of super spreaders is of significant importance. Since hubs become the app-users, this strategy has drastic effects on the size and threshold of the epidemic, such that the threshold get pushed from somewhere near zero to a value $\bar{k} > 5$ with the app adoption rate $\pi_a = 0.8$. Therefore, the reproduction number can be much more controlled in the high-degree targeting strategy.

D. The effect of homophily and heterophily

In previous sections, there was an assumption that app-users are disturbed with random mixing patterns; the fact that one of the connections of a node is an app-user has no effect on the probability of that node being an app adopter. Next, we explore how homophily/heterophily affects the epidemics based on the app usage.

The Fig. 5 illustrates that increasing heterophily leads to lower epidemic threshold and larger epidemics for a fixed \bar{k} . Increasing homophily from random mixing is initially preferable, but the optimum lies between random mixing and full homophily. For the expected epidemic size, strong heterophily is especially detrimental

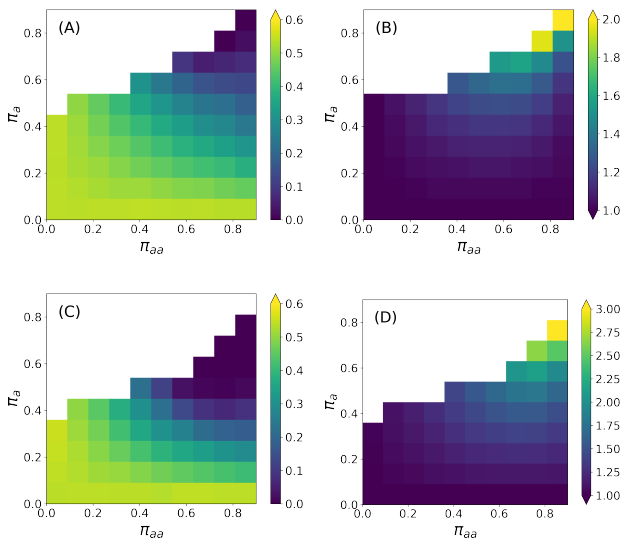


FIG. 5. The effect of homophily/heterophily in app adoption in homogeneous networks. Expected epidemic size at $\bar{k} = 1.8$ for (a) random app adoption and for (c) high-degree targeting strategy. Epidemic threshold for (b) random app adoption and for (d) the high-degree targeting strategy. Thresholds are from theoretical results and expected epidemic sizes are from percolation simulations. The empty white region is the spectrum that having such a homo/heterophilic population is impossible.

(see Fig. 5a for the homogeneous network and with random app adoption and in Fig. 5c for high-degree targeting strategy). The optimum value for heterophily/homophily is especially visible for the epidemic thresholds in Fig. 5b and Fig. 5d, respectively, for the random and high-degree targeting strategies. Fig. 6b gives a more clear picture of existence of an optimum value for the epidemic threshold in the case of homophily. According to Eq. 23, for each fraction of app-users π_a in the network, the epidemic threshold $\bar{k}^c(\pi_a, \pi_{aa})$ can be maximised by controlling the homophily in app adoption π_{aa} . The pattern in the Fig. 6b is very similar to the convex pattern in Fig. 5b, even though they are calculated using different approximations and approaches (see Sec. II A and Sec. II B).

Another view on the effect of homophily and heterophily is given by finding the critical fraction app-users π_a^c that is needed to go beyond the epidemic threshold as function of $(\pi_{aa}$ and $\bar{k})$. Fig. 6a depicts this relationship based on Eq. 25 and shows that π_a^c is not monotonic function of $(\pi_{aa}$ but there is an optimal value of $(\pi_{aa}$ giving a lowest fraction apps that are needed to stop the epidemic. Note that in a network without homophily or heterophily π_a^c increases monotonically as the function of the effective connectivity \bar{k} (see the inset of Fig. 6a).

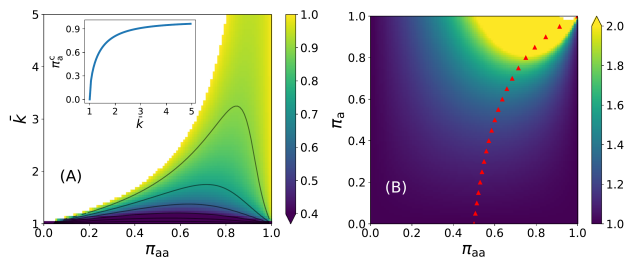


FIG. 6. Existence of optimum value for homophily based on branching process approximation. (a) The critical value of app users π_a^c that are needed for reducing the reproductive number as a function of effective connectivity and homophily probability π_{aa} . The value of π_a^c remains the same within each black curve. The inset is the graph of π_a^c as a function of \bar{k} in the absence of homophily $\pi_{aa} = \pi_a$ given by Eq. 26. (b) The epidemic threshold \bar{k} as a function of π_{aa} and π_a . The red symbols show the π_{aa}^{opt} for each π_a which is given by to Eq. 24. The pattern here is consistent with another approximation which is show in Fig. 5b, while epidemic threshold values are slightly different due to different levels of approximations. Note that here we display the epidemic threshold for all values of π_{aa} and π_a even if networks with some of these parameters cannot be created in practise [89] as indicated by the white regions in Fig. 5b.

IV. DISCUSSIONS

In this article we have developed two flexible analytic approximations to SIR epidemics in the presence of contact tracing apps. First, we use a branching processes to derive explicit analytical solutions for the epidemic thresholds. Second, we expand the framework of using consistency equations to analyze digital contact tracing [41], which is an alternative to other approaches [70]. Contrary to the conventional SIR spreading, a full picture of the late-state epidemics in the presence of digital contact tracing is not given by a single observable (the component size) but one also needs two variables (normal and extended component sizes). These correspond to the probability of the epidemic and the epidemic size, which are equivalent in the SIR process. Here we see that the two quantities can be significantly different if the number of application users is high.

Our numerical work illustrates that the results of digital contact tracing can be very sensitive to the network structure, how applications are distributed among the population and how well the tracing works. That is, realistic estimates of the effects of digital contact tracing can only be achieved if one is able to choose correct parameter ranges in a high-dimensional parameter space. In this study, we had 6 of such parameters: shape of the degree distribution, average degree, amount of heterophily/homophily, application prevalence, quarantine probability and targeting strategy. While we were able to establish and confirm basic laws governing individual parameters and some combinations of parameters, exploring such a parameter space fully for possible compound

effects is out of the reach in simulations. However, these types of effects can be largely revealed by inspecting the analytic equations we derived.

There are several open questions for which the results are only hinted by this study and other studies. Clearly, there are types of network structures we ignore here. For example, the heterophily and homophily could be constructed in the network in slightly different ways. From a practical point of view, one could create networks based on real age-based contact structures and digital contact tracing prevalence and estimate the benefits of applications relative to the risk groups.

Overall the problem of digital contact tracing offers not only a practical problem to solve, but an interesting theoretical puzzle, because it introduces memory to the epidemic process. This memory is limited to one step within the tracing model we use here, but one could also use multi-step tracing, where also the second neighbors of infected nodes are quarantined in the case that the first neighbors have already passed on the infection.

Further, here we ignore effects such as quarantines that do not directly stop the infection from one application user to another from spreading further. However, in the case that there is a strong group structure in the network, there could be for example situations where a non-application user A infects application user B who alerts another application user C, who actually gets infected by A and stops the spreading because of the quarantine. Analyzing such more complicated phenomena can provide challenges for network scientists for years to come.

ACKNOWLEDGEMENT

The simulations presented above were performed using computer resources within the Aalto University School of Science “Science-IT” project. AF acknowledges funding by Science Foundation Ireland Grant No. 16/IA/4470, No. 16/RC/3918, No. 12/RC/2289P2 and No. 18/CRT/6049.

-
- [1] N. Perra, Non-pharmaceutical interventions during the covid-19 pandemic: A review, *Physics Reports* <https://doi.org/10.1016/j.physrep.2021.02.001> (2021).
- [2] Y. Cheng, N. Ma, C. Witt, S. Rapp, P. S. Wild, M. O. Andreae, U. Pöschl, and H. Su, Face masks effectively limit the probability of sars-cov-2 transmission, *Science* (2021).
- [3] M. J. Keeling and P. Rohani, *Modeling infectious diseases in humans and animals* (Princeton university press, 2011).
- [4] W. H. Foegen, J. D. Millar, and J. M. Lane, Selective epidemiologic control in smallpox eradication, *American journal of epidemiology* **94**, 311 (1971).
- [5] K. C. Swanson, C. Altare, C. S. Wessleh, T. Nyenswah, T. Ahmed, N. Eyal, E. L. Hamblion, J. Lessler, D. H. Peters, and M. Altmann, Contact tracing performance during the ebola epidemic in liberia, 2014-2015, *PLoS neglected tropical diseases* **12**, e0006762 (2018).
- [6] G. W. Rutherford and J. M. Woo, Contact tracing and the control of human immunodeficiency virus infection, *JAMA* **259**, 3609 (1988).
- [7] G. J. Fox, S. E. Barry, W. J. Britton, and G. B. Marks, Contact investigation for tuberculosis: a systematic review and meta-analysis, *European Respiratory Journal* **41**, 140 (2013).
- [8] A. Aleta, D. Martin-Corral, A. P. y Piontti, M. Ajelli, M. Litvinova, M. Chinazzi, N. E. Dean, M. E. Halloran, I. M. Longini Jr, S. Merler, *et al.*, Modelling the impact of testing, contact tracing and household quarantine on second waves of covid-19, *Nature Human Behaviour* **4**, 964 (2020).
- [9] P. G. Walker, C. Whittaker, O. J. Watson, M. Baguelin, P. Winskill, A. Hamlet, B. A. Djafaara, Z. Cucunubá, D. O. Mesa, W. Green, *et al.*, The impact of covid-19 and strategies for mitigation and suppression in low-and middle-income countries, *Science* **369**, 413 (2020).
- [10] S. M. Kissler, C. Tedijanto, E. Goldstein, Y. H. Grad, and M. Lipsitch, Projecting the transmission dynamics of sars-cov-2 through the postpandemic period, *Science* **368**, 860 (2020).
- [11] J. Bell, G. Bianconi, D. Butler, J. Crowcroft, P. C. Davies, C. Hicks, H. Kim, I. Z. Kiss, F. Di Lauro, C. Maple, *et al.*, Beyond covid-19: network science and sustainable exit strategies, *Journal of Physics: Complexity* **2**, 021001 (2021).
- [12] M. Gilbert, M. Dewatripont, E. Muraille, J.-P. Platteau, and M. Goldman, Preparing for a responsible lockdown exit strategy, *Nature medicine* **26**, 643 (2020).
- [13] N. E. Kogan, L. Clemente, P. Liautaud, J. Kaashoek, N. B. Link, A. T. Nguyen, F. S. Lu, P. Huybers, B. Resch, C. Havas, A. Petutschnig, J. Davis, M. Chinazzi, B. Mustafa, W. P. Hanage, A. Vespignani, and M. Santillana, An early warning approach to monitor covid-19 activity with multiple digital traces in near real time, *Science Advances* **7**, 10.1126/sciadv.abd6989 (2021).
- [14] S. Kojaku, L. Hébert-Dufresne, E. Mones, S. Lehmann, and Y.-Y. Ahn, The effectiveness of backward contact tracing in networks, *Nature Physics* , 1 (2021).
- [15] M. Salathe, L. Bengtsson, T. J. Bodnar, D. D. Brewer, J. S. Brownstein, C. Buckee, E. M. Campbell, C. Cattuto, S. Khandelwal, P. L. Mabry, *et al.*, Digital epidemiology, *PLoS Comput Biol* **8**, e1002616 (2012).
- [16] A. Natarajan, H.-W. Su, and C. Heneghan, Assessment of physiological signs associated with covid-19 measured using wearable devices, *NPJ digital medicine* **3**, 1 (2020).
- [17] D. R. Seshadri, E. V. Davies, E. R. Harlow, J. J. Hsu, S. C. Knighton, T. A. Walker, J. E. Voos, and C. K. Drummond, Wearable sensors for covid-19: a call to action to harness our digital infrastructure for remote patient monitoring and virtual assessments, *Frontiers in Digital Health* **2**, 8 (2020).
- [18] D. P. Oran and E. J. Topol, Prevalence of asymptomatic sars-cov-2 infection: a narrative review, *Annals of internal medicine* **173**, 362 (2020).

- [19] E. Morales-Narváez and C. Dincer, The impact of biosensing in a pandemic outbreak: Covid-19, *Biosensors and Bioelectronics* **163**, 112274 (2020).
- [20] G. Quer, J. M. Radin, M. Gadaleta, K. Baca-Motes, L. Ariniello, E. Ramos, V. Kheterpal, E. J. Topol, and S. R. Steinhubl, Wearable sensor data and self-reported symptoms for covid-19 detection, *Nature Medicine* **27**, 73 (2021).
- [21] T. Mishra, M. Wang, A. A. Metwally, G. K. Bogu, A. W. Brooks, A. Bahmani, A. Alavi, A. Celli, E. Higgs, O. Dagan-Rosenfeld, *et al.*, Pre-symptomatic detection of covid-19 from smartwatch data, *Nature Biomedical Engineering* **4**, 1208 (2020).
- [22] A. Ganguli, A. Mostafa, J. Berger, M. Y. Aydin, F. Sun, S. A. S. de Ramirez, E. Valera, B. T. Cunningham, W. P. King, and R. Bashir, Rapid isothermal amplification and portable detection system for sars-cov-2, *Proceedings of the National Academy of Sciences* **117**, 22727 (2020).
- [23] P. Fozouni, S. Son, M. D. de León Derby, G. J. Knott, C. N. Gray, M. V. D’Ambrosio, C. Zhao, N. A. Switz, G. R. Kumar, S. I. Stephens, *et al.*, Direct detection of sars-cov-2 using crispr-cas13a and a mobile phone, *MedRxiv* (2020).
- [24] C. Menni, A. Valdes, M. B. Freydin, S. Ganesh, J. E.-S. Moustafa, A. Visconti, P. Hysi, R. C. Bowyer, M. Mangino, M. Falchi, *et al.*, Loss of smell and taste in combination with other symptoms is a strong predictor of covid-19 infection, *MedRxiv* (2020).
- [25] T. Varsavsky, M. S. Graham, L. S. Canas, S. Ganesh, J. C. Pujol, C. H. Sudre, B. Murray, M. Modat, M. J. Cardoso, C. M. Astley, *et al.*, Detecting covid-19 infection hotspots in england using large-scale self-reported data from a mobile application: a prospective, observational study, *The Lancet Public Health* **6**, e21 (2021).
- [26] A. Ganguli, A. Ornob, H. Yu, G. Damhorst, W. Chen, F. Sun, A. Bhuiya, B. Cunningham, and R. Bashir, Hands-free smartphone-based diagnostics for simultaneous detection of zika, chikungunya, and dengue at point-of-care, *Biomedical microdevices* **19**, 1 (2017).
- [27] L. B. Sousa, S. R. Fricker, S. S. Doherty, C. E. Webb, K. L. Baldock, and C. R. Williams, Citizen science and smartphone e-entomology enables low-cost upscaling of mosquito surveillance, *Science of the Total Environment* **704**, 135349 (2020).
- [28] N. G. Becker, K. Glass, Z. Li, and G. K. Aldis, Controlling emerging infectious diseases like sars, *Mathematical biosciences* **193**, 205 (2005).
- [29] M. Eichner, Case isolation and contact tracing can prevent the spread of smallpox, *American journal of epidemiology* **158**, 118 (2003).
- [30] K. T. Eames and M. J. Keeling, Contact tracing and disease control, *Proceedings of the Royal Society of London. Series B: Biological Sciences* **270**, 2565 (2003).
- [31] I. Z. Kiss, D. M. Green, and R. R. Kao, Infectious disease control using contact tracing in random and scale-free networks, *Journal of The Royal Society Interface* **3**, 55 (2006).
- [32] R. M. HOWELL, W. J. Kassler, and A. Haddix, Partner notification to prevent pelvic inflammatory disease in women: cost-effectiveness of two strategies, *Sexually transmitted diseases* **24**, 287 (1997).
- [33] C. Fraser, S. Riley, R. M. Anderson, and N. M. Ferguson, Factors that make an infectious disease outbreak controllable, *Proceedings of the National Academy of Sciences* **101**, 6146 (2004).
- [34] M. Kretzschmar, Y. T. van Duynhoven, and A. J. Severijnen, Modeling prevention strategies for gonorrhoea and chlamydia using stochastic network simulations, *American Journal of Epidemiology* **144**, 306 (1996).
- [35] D. Klinkenberg, C. Fraser, and H. Heesterbeek, The effectiveness of contact tracing in emerging epidemics, *PLoS one* **1**, e12 (2006).
- [36] R. Huerta and L. S. Tsimring, Contact tracing and epidemics control in social networks, *Phys. Rev. E* **66**, 056115 (2002).
- [37] P. Rodríguez, S. Graña, E. E. Alvarez-León, M. Battaglini, F. J. Darias, M. A. Hernán, R. López, P. Llaneza, M. C. Martín, O. Ramirez-Rubio, *et al.*, A population-based controlled experiment assessing the epidemiological impact of digital contact tracing, *Nature communications* **12**, 1 (2021).
- [38] I. Braithwaite, T. Callender, M. Bullock, and R. W. Aldridge, Automated and partly automated contact tracing: a systematic review to inform the control of covid-19, *The Lancet Digital Health* (2020).
- [39] M. Salathé, C. L. Althaus, N. Anderegg, D. Antonioli, T. Ballouz, E. Bugnion, S. Capkun, D. Jackson, S.-I. Kim, J. Larus, *et al.*, Early evidence of effectiveness of digital contact tracing for sars-cov-2 in switzerland, *medRxiv* (2020).
- [40] J. O’Connell and D. T. O’Keeffe, Contact tracing for covid-19—a digital inoculation against future pandemics, *New England Journal of Medicine* (2021).
- [41] A. Barrat, C. Cattuto, M. Kivelä, S. Lehmann, and J. Saramäki, Effect of manual and digital contact tracing on covid-19 outbreaks: a study on empirical contact data, *medRxiv* 10.1101/2020.07.24.20159947 (2020).
- [42] E. Shim, A. Tariq, W. Choi, Y. Lee, and G. Chowell, Transmission potential and severity of covid-19 in south korea, *International Journal of Infectious Diseases* **93**, 339 (2020).
- [43] J. Cohen and K. Kupferschmidt, Countries test tactics in ‘war’ against covid-19 (2020).
- [44] G. Cencetti, G. Santin, A. Longa, E. Pigani, A. Barrat, C. Cattuto, S. Lehmann, M. Salathe, and B. Lepri, Digital proximity tracing on empirical contact networks for pandemic control, *medRxiv*, 2020 (2021).
- [45] H. L. Hambridge, R. Kahn, and J.-P. Onnela, Examining sars-cov-2 interventions in residential colleges using an empirical network, *medRxiv* 10.1101/2021.03.09.21253198 (2021).
- [46] C. Wymant, L. Ferretti, D. Tsallis, M. Charalambides, L. Abeler-Dörner, D. Bonsall, R. Hinch, M. Kendall, L. Milsom, M. Ayres, *et al.*, The epidemiological impact of the nhs covid-19 app, *Alan Turing Institute: London, UK* (2021).
- [47] R. Pastor-Satorras and A. Vespignani, *Evolution and structure of the Internet: A statistical physics approach* (Cambridge University Press, 2007).
- [48] S. N. Dorogovtsev and J. F. Mendes, *Evolution of networks: From biological nets to the Internet and WWW* (OUP Oxford, 2013).
- [49] R. Albert and A.-L. Barabási, Statistical mechanics of complex networks, *Reviews of modern physics* **74**, 47 (2002).
- [50] R. Pastor-Satorras and A. Vespignani, Epidemic spreading in scale-free networks, *Physical review letters* **86**, 3200 (2001).

- [51] D. Centola, An experimental study of homophily in the adoption of health behavior, *Science* **334**, 1269 (2011).
- [52] S. Funk, M. Salathé, and V. A. Jansen, Modelling the influence of human behaviour on the spread of infectious diseases: a review, *Journal of the Royal Society Interface* **7**, 1247 (2010).
- [53] V. von Wyl, M. Höglinger, C. Sieber, M. Kaufmann, A. Moser, M. Serra-Burriel, T. Ballouz, D. Menges, A. Frei, and M. A. Puhán, Drivers of acceptance of covid-19 proximity tracing apps in switzerland: panel survey analysis, *JMIR public health and surveillance* **7**, e25701 (2021).
- [54] J. A. M. López, B. A. García, P. Bentkowski, L. Bioglio, F. Pinotti, P.-Y. Boëlle, A. Barrat, V. Colizza, and C. Poletto, Anatomy of digital contact tracing: role of age, transmission setting, adoption and case detection, *Science Advances*, eabd8750 (2021).
- [55] M. Newman, *Networks* (Oxford university press, 2018).
- [56] L. Hébert-Dufresne, B. M. Althouse, S. V. Scarpino, and A. Allard, Beyond r_0 : heterogeneity in secondary infections and probabilistic epidemic forecasting, *Journal of the Royal Society Interface* **17**, 20200393 (2020).
- [57] M. Boguná, R. Pastor-Satorras, and A. Vespignani, Absence of epidemic threshold in scale-free networks with degree correlations, *Physical review letters* **90**, 028701 (2003).
- [58] M. Barthélemy, A. Barrat, R. Pastor-Satorras, and A. Vespignani, Velocity and hierarchical spread of epidemic outbreaks in scale-free networks, *Physical review letters* **92**, 178701 (2004).
- [59] R. Pastor-Satorras and A. Vespignani, Epidemic dynamics in finite size scale-free networks, *Physical Review E* **65**, 035108 (2002).
- [60] S. Dhara, R. van der Hofstad, and J. S. van Leeuwen, Critical percolation on scale-free random graphs: new universality class for the configuration model, *Communications in Mathematical Physics*, 1 (2021).
- [61] L. Ferretti, C. Wymant, M. Kendall, L. Zhao, A. Nurtay, L. Abeler-Dörner, M. Parker, D. Bonsall, and C. Fraser, Quantifying sars-cov-2 transmission suggests epidemic control with digital contact tracing, *Science* **368** (2020).
- [62] P. Sapiezynski, J. Pruessing, and V. Sekara, The fallibility of contact-tracing apps, *arXiv preprint arXiv:2005.11297* (2020).
- [63] Y. Liu, R. M. Eggo, and A. J. Kucharski, Secondary attack rate and superspreading events for sars-cov-2, *The Lancet* **395**, e47 (2020).
- [64] Z. Shen, F. Ning, W. Zhou, X. He, C. Lin, D. P. Chin, Z. Zhu, and A. Schuchat, Superspreading sars events, beijing, 2003, *Emerging infectious diseases* **10**, 256 (2004).
- [65] S. Cléménçon, H. De Arazoza, F. Rossi, and V. C. Tran, A statistical network analysis of the hiv/aids epidemics in cuba, *Social Network Analysis and Mining* **5**, 1 (2015).
- [66] J. O. Lloyd-Smith, S. J. Schreiber, P. E. Kopp, and W. M. Getz, Superspreading and the effect of individual variation on disease emergence, *Nature* **438**, 355 (2005).
- [67] K. Kupferschmidt, Why do some covid-19 patients infect many others, whereas most don't spread the virus at all, *Science* **10** (2020).
- [68] S. L. Feld, Why your friends have more friends than you do, *American Journal of Sociology* **96**, 1464 (1991).
- [69] M. E. Newman, Threshold effects for two pathogens spreading on a network, *Physical review letters* **95**, 108701 (2005).
- [70] G. Bianconi, H. Sun, G. Rapisardi, and A. Arenas, Message-passing approach to epidemic tracing and mitigation with apps, *Physical Review Research* **3**, L012014 (2021).
- [71] I. Kryven and C. Stegehuis, Contact tracing in configuration models, *Journal of Physics: Complexity* **2**, 025004 (2021).
- [72] A. Allard, C. Moore, S. V. Scarpino, B. M. Althouse, and L. Hébert-Dufresne, The role of directionality, heterogeneity and correlations in epidemic risk and spread, *arXiv:2005.11283* (2020).
- [73] R. B. Simões, I. Amaral, and S. Santos, Tracking the outbreak and far beyond: How are public authorities using mobile apps to control covid-19 pandemic, *Multidisciplinary Perspectives of Communication in a Pandemic Context* **1**, 166 (2021).
- [74] M. Abueg, R. Hinch, N. Wu, L. Liu, W. J. Probert, A. Wu, P. Eastham, Y. Shafi, M. Rosencrantz, M. Dikovsky, *et al.*, Modeling the combined effect of digital exposure notification and non-pharmaceutical interventions on the covid-19 epidemic in washington state, *medRxiv* (2020).
- [75] A. Bassolas, A. Santoro, S. Sousa, S. Rognone, and V. Nicosia, Optimising the mitigation of epidemic spreading through targeted adoption of contact tracing apps, *arXiv:2102.13013* (2021).
- [76] M. Kendall, L. Milsom, L. Abeler-Dörner, C. Wymant, L. Ferretti, M. Briers, C. Holmes, D. Bonsall, J. Abeler, and C. Fraser, Epidemiological changes on the isle of wight after the launch of the nhs test and trace programme: a preliminary analysis, *The Lancet Digital Health* **2**, e658 (2020).
- [77] G. Burgio, B. Steinegger, G. Rapisardi, and A. Arenas, The impact of homophily on digital proximity tracing, *arXiv:2103.00635* (2021).
- [78] M. E. Newman, Spread of epidemic disease on networks, *Physical review E* **66**, 016128 (2002).
- [79] R. Pastor-Satorras, C. Castellano, P. Van Mieghem, and A. Vespignani, Epidemic processes in complex networks, *Reviews of modern physics* **87**, 925 (2015).
- [80] R. Albert, H. Jeong, and A.-L. Barabási, Error and attack tolerance of complex networks, *nature* **406**, 378 (2000).
- [81] R. Cohen, K. Erez, D. Ben-Avraham, and S. Havlin, Resilience of the internet to random breakdowns, *Physical review letters* **85**, 4626 (2000).
- [82] A. Barrat, M. Barthélemy, and A. Vespignani, *Dynamical processes on complex networks* (Cambridge university press, 2008).
- [83] S. N. Dorogovtsev, A. V. Goltsev, and J. F. Mendes, Critical phenomena in complex networks, *Reviews of Modern Physics* **80**, 1275 (2008).
- [84] L. Basnarkov, M. Mirchev, and L. Kocarev, Random walk with memory on complex networks, *Physical Review E* **102**, 042315 (2020).
- [85] P. Shu, Effects of memory on information spreading in complex networks, in *2014 IEEE 17th International Conference on Computational Science and Engineering (IEEE, 2014)* pp. 554–556.
- [86] E. Kenah and J. M. Robins, Second look at the spread of epidemics on networks, *Physical Review E* **76**, 036113 (2007).
- [87] E. Kenah and J. C. Miller, Epidemic percolation networks, epidemic outcomes, and interventions, *Interdisci-*

- plinary perspectives on infectious diseases **2011** (2011).
 [88] B. Bollobás and B. Béla, *Random graphs*, 73 (Cambridge university press, 2001).
 [89] J. P. Gleeson, Cascades on correlated and modular random networks, *Phys. Rev. E* **77**, 046117 (2008).

APPENDIX

About quarantine failures, as it was shown in Fig. 3, Fig. 7 and 8 also show that contact tracing can yield very good results in terms of reducing the epidemic threshold and expected epidemic size if every thing goes right at least for 50% and half of the people use the apps. This effect is larger if we go for the high-degree targeting strategy especially in heterogeneous networks as is shown in Fig. 7d and 8d. Fig. 9 and 10 show that there is an optimum value for homophily in app adoption as it was shown in Fig. 5 and Fig. 6. The only exception is when we follow high-degree targeting strategy in heterogeneous networks. In this case we can see the hub effect on the epidemic threshold and size.

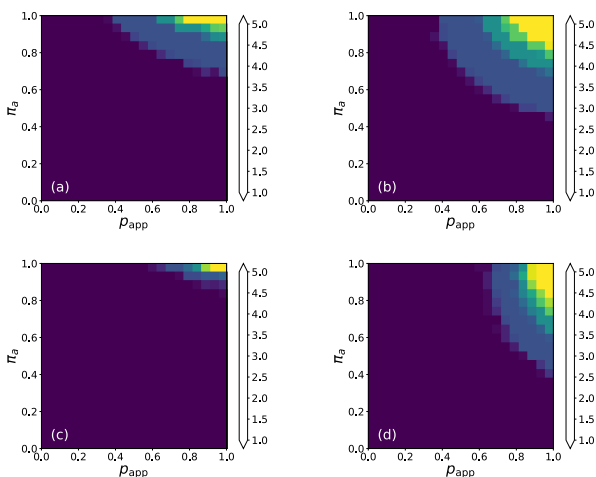


FIG. 7. The epidemic threshold as a function of quarantine probability p_{app} and app adoption rate π_a . The effect of quarantine failures in homogeneous networks with (a) random app adoption (b) and high-degree targeting strategy. Also for heterogeneous networks with a power-law degree distribution with (c) random app adoption (d) and high-degree targeting strategy. All threshold values larger than 5 are shown with the same color.

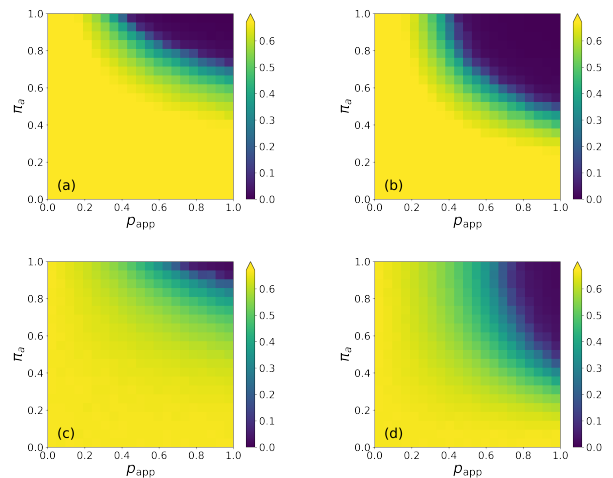


FIG. 8. Expected epidemic size in the case of quarantine failures. Expected epidemic size at $\bar{k} = 1.8$ for homogeneous networks with (a) random app adoption (b) and high-degree targeting strategy. Also for heterogeneous networks with a power-law degree distribution with (c) random app adoption (d) and high-degree targeting strategy. In (b) and (d) the pattern is different due to the effects of hubs. When doing high-degree targeting strategy, quarantine failures are more significant since the infected ones are highly influential on the dynamics of the spreading.

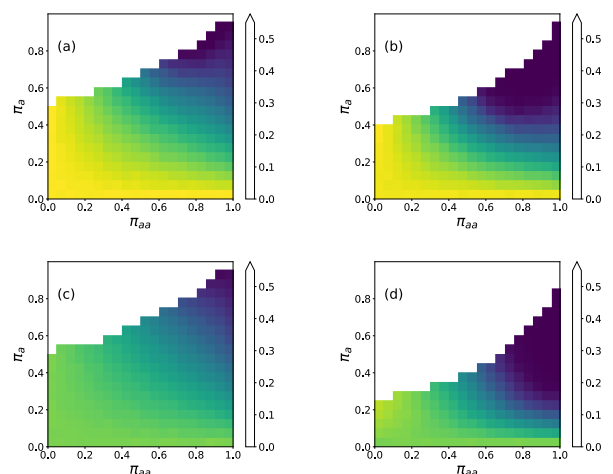


FIG. 9. The effect of homophily/heterophily in app adoption on the expected epidemic size. Expected epidemic size at $\bar{k} = 1.8$ from percolation simulations for homogeneous networks with (a) random app adoption (b) and high-degree targeting strategy. Also for heterogeneous networks with a power-law degree distribution with (c) random app adoption (d) and high-degree targeting strategy. The empty white region is the spectrum that having such a homo/heterophilic population is impossible.

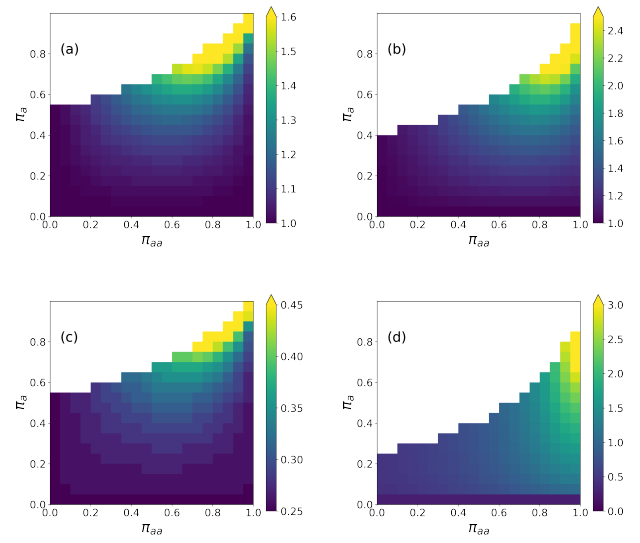


FIG. 10. The effect of homophily/heterophily in app adoption on the epidemic threshold and optimum pattern for homophily. Epidemic thresholds for homogeneous networks with (a) random app adoption (b) and high-degree targeting strategy. Also for heterogeneous networks with a power-law degree distribution with (c) random app adoption (d) and high-degree targeting strategy. The empty white region is the spectrum that having such a homo/heterophilic population is impossible.

Magnetic properties of BaCuTe₂O₆

X-ray diffraction, thermodynamic measurements, and density-functional band-structure calculations are used to study the magnetic behavior of BaCuTe₂O₆, a member of the ACuTe₂O₆ structural family that hosts complex three-dimensional frustrated spin networks with possible spin-liquid physics. Temperature-dependent magnetic susceptibility and heat capacity of the Ba compound are well described by the one-dimensional spin-1/2 Heisenberg chain model reminiscent of the Sr-analog SrCuTe₂O₆. While the intrachain coupling $J/k_B \approx 37\text{K}$ is reduced compared to 49 K in the Sr compound, the Néel temperature increases from 5.5 K (Sr) to 6.1 K (Ba). Unlike the Sr compound, BaCuTe₂O₆ undergoes only one magnetic transition as a function of temperature and shows signatures of weak spin canting. We elucidate the microscopic difference between the Sr and Ba compounds and suggest that one of the interchain couplings changes sign as a result of negative pressure caused by the Sr/Ba substitution. The Néel temperature of BaCuTe₂O₆ is remarkably insensitive to the magnetic dilution with Zn²⁺ up to the highest reachable level of about 20 %.

Analytic continuation over complex landscapes

Continuation of models to complex parameters or phase space integrals to complex degrees of freedom is useful in a variety of contexts—for defining an otherwise divergent theory or ameliorating the sign problem in Monte Carlo—and relies on knowledge of the critical points of the energy landscape. We study complex continuation of models with complex, or 'rugged,' energy landscapes. Unlike real landscapes, there is no useful classification of saddles by index. Instead, the spectrum at critical points determines their tendency to trade topological numbers under continuation. These trades, which occur at Stokes points, proliferate when the spectrum includes marginal directions and are exponentially suppressed otherwise. This gives a direct interpretation of the 'threshold' energy—which in the real case separates saddles from minima—where the spectrum of typical critical points develops a gap. This leads to different consequences for the analytic continuation of real landscapes with different structures: the global minima of "one step replica-symmetry broken" landscapes lie beyond a threshold and are locally protected from Stokes points, whereas those of "many step replica-symmetry broken" lie at the threshold and Stokes points immediately proliferate.

Thermodynamics of structure-forming systems

Structure-forming systems are ubiquitous in nature, ranging from atoms building molecules to self-assembly of colloidal amphibolic particles. The understanding of the underlying thermodynamics of such systems remains an important problem. Here, we derive the entropy for structure-forming systems that differs from Boltzmann-Gibbs entropy by a term that explicitly captures clustered states. For large systems and low concentrations the approach is equivalent to the grand-canonical ensemble; for small systems we find significant deviations. We derive the detailed fluctuation theorem and Crooks' work fluctuation theorem for structure-forming systems. The connection to the theory of particle self-assembly is discussed. We apply the results to several physical systems. We present the phase diagram for patchy particles described by the Kern-Frenkel potential. We show that the Curie-Weiss model with molecule structures exhibits a first-order phase transition. Reference: Nature Communications 12 (2021) 1127.

Irreversibility, heat and information flows induced by non-reciprocal interactions

In complex systems far from equilibrium, such as active matter, Newton's third law does not always hold, giving rise to non-reciprocal interactions. Here, we study the thermodynamic properties induced by non-reciprocal interactions between stochastic degrees of freedom. We show that non-reciprocal coupling alone implies a steady energy flow through the system, as well as a nontrivial information flow. Remarkably, non-reciprocal coupling can induce a reversed heat flow from cold to hot. We also discuss the dynamics and thermodynamics seen by a marginal observer, who only sees one of two non-reciprocally coupled systems. We show that, due to the non-reciprocity, the non-Markovian dynamics seen by the marginal observer involves complex types of memory, and that the marginal entropy production obeys a generalized second law involving the information flow. [SAM Loos, SHL Klapp, NJP 22, 123051 (2020).]

Thermodynamics of Gambling Demons

The stochastic nature of games at the casino allows lucky players to make profit by means of gambling. Like games of chance and stocks, small physical systems are subject to fluctuations, thus their energy and entropy become stochastic, following an unpredictable evolution. In this context, information about the evolution of a thermodynamic system can be used by Maxwell's demons to extract work using feedback control. This is not always the case, and a challenging task is then to develop efficient thermodynamic protocols achieving work extraction in situations where feedback control cannot be realized, in the same spirit as it is done on a daily basis in casinos and financial markets. We introduce and realize gambling demons who, following a customary gambling strategy to stop a nonequilibrium process at stochastic times, are able to extract more average work than the free energy change. We derive second laws in the presence of gambling, and a set of universal stopping-time fluctuation relations for the work done in classical and quantum stochastic non-stationary processes. We test experimentally our results in a single-electron box, where an electrostatic potential is used to drive the dynamics of individual electrons tunneling into a metallic island.

Study of electronic, magnetic and magnetocaloric properties of double perovskites

R. Masrour, A. Jabar

Laboratory of Solid Physics, Faculty of Sciences Dhar El Mahraz, Sidi Mohamed Ben

Abdellah University, BP 1796, Fez, Morocco

Corresponding author:* rachidmasrour@hotmail.com

We have used the density functional theory base on full potential linearized augmented plane wave combined and Monte Carlo Simulation to study the magnetic, electronic and magnetocaloric properties of double perovskites $A_2BB'O_6$ with B, B' and A are metal ions, alkali, alkaline earth or rare earth ions, respectively. The total and partial densities of states for spin up and spins down are found. The thermal magnetization, magnetic susceptibility and specific heat are given. The magnetic entropy change and relative cooling power are found.

Asymmetric coupling of two-channel exclusion process with interactions**Tripti Midha***Department of Mathematics, Akal University, Talwandi Sabo, Punjab, India, 151302*

Molecular motors or motor proteins are enzymatic molecules that support various biological processes such as intracellular transport, cell division, synthesis of proteins, cell motility and signalling. They perform mechanical work by typically converting the chemical energy derived from the hydrolysis of ATP. Experiment evidence suggest that the motors work in parallel channels (microtubules) and undergo various intermolecular interactions. In this work, we examine an open two-channel asymmetrically coupled interactive totally asymmetric simple exclusion process. The model incorporates the inter as well as intra channel interactions in the thermodynamically consistent way. We developed a modified cluster mean-field approach to capture the correlations in the system. The theory can analytically compute the steady-state phase boundaries and phase diagram of the system. We also analytically calculate the correlations and discuss its nature for repulsive and attractive interaction energy. We validate our theoretical results with extensively performed Monte Carlo simulations. Further, the biological significance of the results is also examined.

Adsorption of a confined polymer chain: Exact results

In this paper, we report exact results on the adsorption-desorption phase transition for a confined flexible polymer chain. The chain is confined in-between a pair of attractive impenetrable surfaces/plates; and the adsorption transition point is obtained analytically for the possible values of the plate separation. Our study showed that the adsorption transition point is a function of the confining plate's separation, provided both surface have attractive interaction with the monomers of the chain. We have also obtained exact results for other possible options of the plate-monomer interaction to understand the adsorption-desorption phase transition behavior of the confined polymer chain.

Introduction

A modern method of time series analysis is to map them onto complex networks and analyze these structures, called **visibility graphs** (VG). In this work we have studied the VG generated from time series of epidemic prevalence in the SIS epidemic model on regular and complex networks.

Methods

Given two values (t_a, y_a) and (t_b, y_b) will have visibility, i.e will be connected in the associated graph, if any point (t_c, y_c) between them satisfy [1]

$$y_c < y_b + (y_a - y_b) \frac{(t_b - t_c)}{(t_b - t_a)} \quad (1)$$

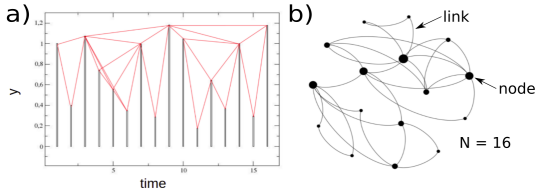


Figure 1: (a) Illustration of the visibility criteria (Eq.(1)) applied to a time series. (b) The VG generated from it, of size $N = 16$ nodes.

We studied the susceptible-infected-susceptible (SIS) epidemic model [2] for different structures.

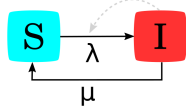


Figure 2: Illustration diagram showing the possible transitions for the SIS epidemic model. A susceptible node i (S) will become infected (I) with probability $k_i \lambda$, with k_i being the node's degree and λ the infection rate. Then, it will become susceptible again with a healing rate μ , fixed as $\mu = 1$ for this work.

Using quasi-stationary methods [3], we generate the time series of epidemic prevalence ρ , which is the fraction of infected individuals in the population as a time function. Varying the infection rate λ of the model, a phase transition in $\langle \rho \rangle$ can be reached in the thermodynamic limit. In Fig.3 an example of the SIS epidemic model in a square lattice is shown.

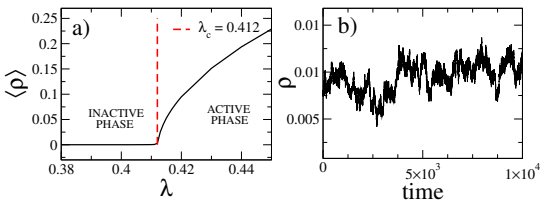


Figure 3: SIS epidemic model in a square lattice of side $n = 500$. (a) Average quasi-stationary epidemic prevalence as a function of the infection rate. (b) Example for time series of epidemic prevalence in the critical region for $\lambda = 0.412$.

Every kind of original networks have different activation mechanisms [4] for the SIS model:

- Regular networks are activated collectively;
- Power law (PL) degree distributed networks, that is $P(k) \sim k^{-\gamma}$, have some structures that activate and sustain the epidemic [5].

In order to study the VG properties, we calculated the **degree correlation** [6], a measure that captures the relationship between the degrees of nodes that link to each other. We evaluated the average degree of the nearest neighbors K_{nn} . Then, we analyzed the K_{nn} as a function of the degree $K_{nn}(k) \sim k^{-\mu}$ [7]. So the degree correlations can be:

- assortative ($\mu > 0$) when nodes of similar degree are connect to each other;
- disassortative ($\mu < 0$) for the inverse situation;
- neutral ($\mu \approx 0$).

After a finite size analysis, all the epidemic prevalence time series (and so the VG) used in this work have size $t = 10^6$. The original networks have size $N = 10^7$, except for the square lattice, with size $N = n^2$ and the 4D lattice $N = n^4$.

Results and Discussion

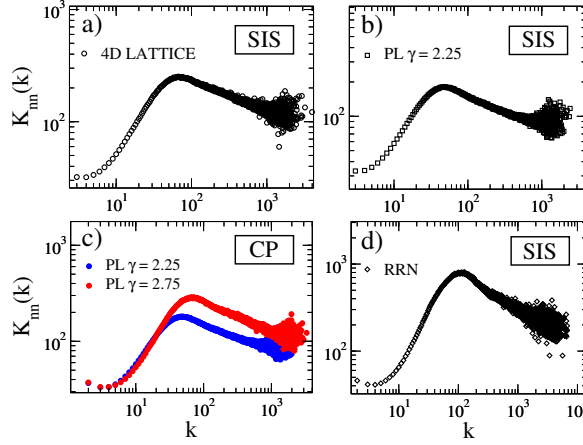


Figure 4: Average neighbors degree for VG generated from critical time series for different models and original networks. (a) SIS model for a 4D lattice of side $n = 32$. (b) SIS model for a PL degree distributed network with $\gamma = 2.25$. (c) CP for PL degree distributed networks with different γ . (d) SIS model in a RRN with degree $k = 4$.

· Networks with strong localization as PL degree distributed with $\gamma > 3$ can exhibit outliers, that are nodes with degree $k_{out} \gg k_{average}$.

· The susceptibility (χ) in Fig.5(a) measures the fluctuations in the order parameter ρ . For values of λ close to the critical point, χ will present a peak.

· In Fig. 5(b) the $K_{nn}(k)$ for the VG are shown. Note that the curves from the first peak are strongly assortative. This peak is related to the outliers presence on the network.

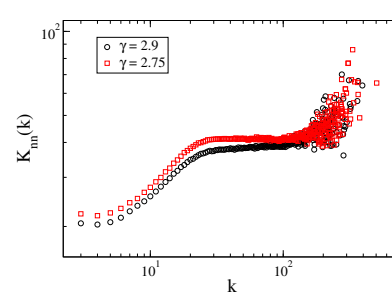


Figure 6: Average neighbors degree for VG generated from critical time series of the SIS epidemic model on PL degree distributed networks.

· For networks with collective activation mechanism the $K_{nn}(k)$ of the VG becomes disassortative for a given k as can be seen in Fig.4.

· The contact process (CP) model is similar to the SIS model but with degree independent infection probability.

· The SIS model in PL degree distributed networks with $\gamma < 2.5$ are activated by the maximum k-core [4].

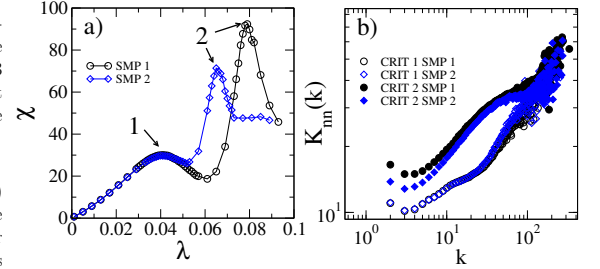


Figure 5: SIS epidemic model on a PL degree distributed network with $\gamma = 3.5$. (a) Susceptibility as a function of infection rate for two different samples, the indications 1 and 2 show the transition points for which the time series were taken. (b) Average neighbors degree for the VG generated from the time series on the critical points.

· Networks with PL degree distribution and $2.5 < \gamma < 3$ are activated by hubs in the SIS epidemic model [5]. But our results show that these networks are not strongly localized neither exhibit collective pattern.

· As can be seen in Fig.6, the average neighbors degree become neutral for a given k , indicating that there is a competition of activation mechanisms.

References

- [1] L. Lacasa *et al.* From time series to complex networks: The Visibility Graph, PNAS, 105(13), 2008.
- [2] R. Pastor-Satorras *et al.* Epidemic Processes in complex networks, RMP, 87(3), 2015.
- [3] R. S. Sander *et al.* Sampling methods for the quasistationary regime of the epidemic processes on regular and complex networks, PRE, 94(4), 2016.
- [4] S.C. Ferreira *et al.* Collective versus hub activation of epidemic phases on networks, PRE, 93(3), 2016.
- [5] W. Cota *et al.* Robustness and fragility of the susceptible-infected-susceptible epidemic models on complex networks, PRE, 98(1), 2018.
- [6] A.L. Barabási, Network Science, Cambridge University Press, 2016.
- [7] R. Pastor-Satorras *et al.* Dynamical and correlation properties of the internet, PRL, 87(25), 2001.
- [8] R. Pastor-Satorras *et al.* Epidemic Spreading in Scale-Free Networks, PRL, 86(14), 2001.

Acknowledgments



Conclusions

Knowing the network architecture where the epidemic spreads is important on the elaboration of strategies for combating the disease [8]. However, in many real cases the network data are not available. In contrast, the values of new cases of a disease are easier to be accessed, and a time series of epidemic prevalence can be constructed. Our results show that the VG degree correlations are connected to the activation mechanism of the original network, becoming more assortative as the localization increases. This indicates that it may be possible to infer information about the original network's structure by analyzing the epidemic time series in the critical regime.

A different way to analyze model membranes

A lipid membrane is a complex system, even when we talk about a *in silico* model. The amphiphilic molecules composing the system have a range of motion over an enormous time span, from picoseconds to hours, for that reason is very hard to study all kind of movements in a molecular dynamic simulation with an all atom representation. Even microseconds simulations can be a challenge in this moment. Considering the difficulty of study this systems, we consider a new approach, in which we use the Pearson Correlation matrix to understand linear correlation between pairs of lipids and we used that information to construct not directed networks. After that, we use some tools from information theory to study non linear correlations and asymmetry in information flow between pairs of lipids. Considering that Transfer entropy is capable of measuring the amount of directed (time-asymmetric) transfer of information between two time series (lipid trajectories), we can use it to gain insight about what agent in the plasma membrane is acting as an influencer and who is acting like influenced.

The quark number susceptibility near the critical transition point in the Phase Transition from a hadronic gas to a colorless QCD plasma

Bachir Moussaoui¹ and Amal Ait El Djoudi¹

¹ Laboratoire de Physique des Particules et Physique Statistique,
Ecole Normale Supérieure-Kouba, B.P. 92, 16050, Vieux-Kouba, Algiers, Algeria
bachir8211@hotmail.fr

Abstract

We study the density driven deconfinement phase transition at fixed temperature T as a function of quark chemical potential μ_q in a finite volume V within the framework of the phase coexistence model. The localization of the critical transition point at fixed T , as a function of μ_q and V is investigated. The study of the quark number susceptibility in finite volume and with the color-singletness condition, is well confirming the first-order of the deconfinement phase transition. This order is determined by calculating the critical exponents relative to the quark number susceptibility as well as to other quantities.

Keywords: Deconfinement phase transition, Quark number susceptibility, Color-singletness, Critical exponents.

Explaining Balanced Triad Statistics in Society by Dyadic Interactions

Triadic interactions often account for the evolution of social (signed) triads towards the so-called balanced state with either three or one positive link. We argue that such balanced triads can also emerge from dyadic interactions if these interactions are determined by homophily between agents. Without knowledge of triads in their neighbourhoods, agents modify their opinions so as to minimize an individual social tension defined via the weighted sum of opinion overlaps with friends and opinion discordance with enemies. The model exhibits a transition from unbalanced to balanced society at a critical temperature which depends on the number of opinions, G , the mean degree, K , and the relative strength of positive interactions to that of negative ones, α . When α exceeds $1/2$ at fixed temperature, a transition between steady states with different fractions of balanced triads occurs.

Non-reciprocal mechanics of crystals violating Newton's third law

The effective interactions between the constituents of driven and active soft matter generically defy Newton's third law. Combining simulations and theory, we showed that microscopic forces violating action-reaction principles cannot stabilize crystalline order on their own. When competing with conventional potential interactions in 2D isotropic solids, non-reciprocal forces define six classes of mechanical responses with no counterparts in equilibrium crystals, all turning otherwise quiescent dislocations into motile singularities.

Structure of Wavefunction for Many-Boson Systems in Mean-Field with Random k-Body Interactions

Recent experimental developments on ultra-cold atoms have renewed interest in theoretical investigations on problems like Bose Einstein condensation, quantum many-body chaos and thermalization in finite interacting many-particle complex quantum systems. This requires analysis of wavefunction properties, for which it is crucial to examine the so-called strength functions (or local density of states) in detail as they give information about how a particular basis state spreads onto the eigenstates. The chaos measures like number of principal components (NPC), information entropy, fidelity decay etc. can also be determined by examining general features of the strength functions. Recently, q-Hermite polynomials have been employed to study spectral densities of SYK model and the Gaussian to semi-circle transition in spectral density follows q-normal distribution (f_{qN}). Recently for fermion systems it is shown that conditional q-normal density (f_{CqN}) can be used to represent strength functions in thermalization region. We analyze wavefunction structure for interacting bosons in presence of a mean-field using embedded random matrix ensembles of k-body interactions. The Hamiltonian H is a sum of one-body $h(1)$ and an embedded Gaussian Orthogonal Ensemble (GOE) of k-body interaction $V(k)$ with interaction strength λ (denoted by BEGOE (1+k)). A complete analytical description of variance of strength function as a function of λ and k is derived and marker λ_t defining thermalization region is obtained. In thermalization region ($\lambda > \lambda_t$), f_{CqN} describes Gaussian to semi-circle transition in strength functions as body rank k of interaction increases. This interpolating form of strength function is utilized to obtain smooth form for NPC.

Liquid-Solid fluidized bed CFD-DEM simulation and validation by Radioactive Particle Tracking

Salierno, Gabriel^{1,2}; Maestri, Mauricio^{1,2}; Picabea, Julia^{1,2}; Cassanello, Miryan^{1,2}
Cardona, María Angélica³; Hojman, Daniel³; Somacal, Hector^{3,4}

¹ Laboratorio de Reactores y Sistemas para la Industria (LARS), Universidad de Buenos Aires, Facultad de Ciencias Exactas y Naturales, Dto. de Industrias, Buenos Aires, Argentina. (miryan@di.fcen.uba.ar)

² CONICET - Universidad de Buenos Aires, Instituto de Tecnología de Alimentos y Procesos Químicos (ITAPROQ), Buenos Aires, Argentina.

³ Laboratorio de Diagnóstico por Radiaciones-LaDiR, Dep. Física Experimental, Comisión Nacional de Energía Atómica (CNEA), San Martín, Buenos Aires, Argentina

⁴ Escuela de Ciencia y Tecnología, Universidad Nacional de San Martín, Buenos Aires.



1) Introduction

Many catalytic processes and operations in the chemical and related industries are carried out in liquid-solid fluidized beds (LSFB). Information of their underlying dynamics is fundamental for proper design of the units and for implementing strategies of process intensification. Moreover, the validation of LSFB modeling to estimate their performance requires comparison with experimental results.

3) Experimental section

Experiments are carried out in an acrylic three-phase fluidized bed (1.2 m height and 0.1 m inner diameter), provided with a liquid distributor, mounted onto a structure jointly to an array of 16 (2"x2") NaI(Tl) scintillation detectors (Fig.1).

Calcium alginate gel beads of 4mm mean diameter is the solid phase (Table 1). The liquid, a dilute solution of CaCl₂ (0.05M), flows at 2,4 cm/s. The solid holdup at rest is 10% and the solid to liquid density ratio is 1.01. The tracer path is followed for several hours (Fig. 4 right) with a sampling period of 30 ms.

For the reconstruction, a calibration stage was carried out previously by measuring the counts when the tracer is positioned at known coordinates within the system.

Using the signal distribution, the tracer radioactivity, the media attenuation coefficient and the dead time of the detection system were fitted for each detector to estimate their response and vinculate it with the mean tracer position within the sampling period [1]. Fig. 4 (right) shows portions of trajectories reconstructed from RPT data.

The column is discretized in voxels and the velocity of the tracer whenever crossing each voxel is computed. Then, the velocities obtained for each voxel are time averaged to get the experimental 3D averaged velocity field (Fig. 5).

	δ (Kg/m ³)	dp (mm)	μ (mPa.s)
Liquid	1018	----	1.07
Solid	1027	4.1 ± 0.5	----
Tracer	1025	5	----

Table 1: System properties.

2) Objective

The objective of this work is to compare experimental results obtained with Radioactive Particle Tracking (RPT) in a pilot scale LSFB with those predicted by a Computational Fluid Dynamics coupled with Discrete Element Method (CFD-DEM). The motion of calcium alginate spheres induced by the upward flow of water in a cylindrical column (Fig. 1) is examined.

Simulation of the liquid and solid motion is solved using the CFDEM coupling software.

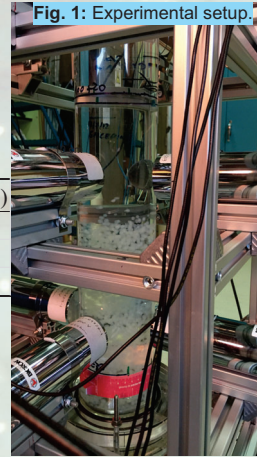


Fig. 1: Experimental setup.

Radioactive tracer (Fig.2) is made of gamma ray source (Fig. 3), inserted in a sphere made of polypropylene (PPP). After activation by neutron bombardment, the tracer is covered with sodium alginate and then polymerized in aqueous CaCl₂ [1].

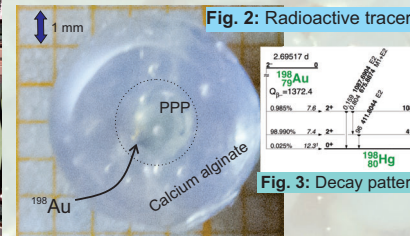


Fig. 2: Radioactive tracer.

Fig. 3: Decay pattern.

5) Force models

The model [2] proposes a strategy to calculate the exchange of momentum between the two phases present; (Eq. 1) and the position and velocity of each of the solid particles (Eqs. 2 and 7).

$$[(\rho_f \varepsilon_i \mathbf{u}) / \partial t + \nabla \cdot (\rho_f \varepsilon_i \mathbf{u} \mathbf{u}) = -\nabla p - [n \mathbf{f}_i / \varepsilon_i - \rho_i \varepsilon_i \mathbf{g}] + \nabla \cdot \boldsymbol{\tau} + \rho_i \varepsilon_i \mathbf{g}$$

Eq. 1: momentum change (liquid phase)

ρ_f ; ρ_s ; ε_f ; ε_s are density and volumetric fractions of fluid and solid respectively \mathbf{u} is the local average velocity of liquid, n is the local number of particles per unit volume, \mathbf{f}_i is the local average force on the particles, p is the local liquid pressure field, $\boldsymbol{\tau}$ is the stress tensor, and \mathbf{g} is the acceleration of gravity.

$$m_i \frac{d\mathbf{v}_i}{dt} = m_i \mathbf{g} + \mathbf{f}_{pf,i} + \sum_{j=1}^{k_c} (\mathbf{f}_{c,ij} + \mathbf{f}_{d,ij})$$

Eq. 2: particle linear momentum change

$$\mathbf{f}_{pf,i} = \mathbf{f}_{\nabla p,i} + \mathbf{f}_{d,i} + \mathbf{f}_{\nabla \cdot \boldsymbol{\tau},i}$$

Eq. 3: particle-fluid interaction

Interparticle collision (plastic component) (elastic component)

$$\mathbf{f}_{\nabla \cdot \boldsymbol{\tau},i} = -(\nabla p) \cdot \mathbf{V}_{p,i}$$

Eq. 4: buoyancy + fluid pressure gradient force

$$\mathbf{f}_{\nabla \cdot \boldsymbol{\tau},i} = -(\nabla \cdot \boldsymbol{\tau}) \mathbf{V}_{p,i}$$

Eq. 5: shear force

$$\mathbf{f}_{d,i} = 0.125 \cdot C_d \cdot \rho_f \pi d_i^2 \varepsilon_i^{2-\chi} \cdot |\mathbf{u}_i - \mathbf{v}_i| (\mathbf{u}_i - \mathbf{v}_i)$$

$$C_d = (0,63 + 4,8/Re_i^{1/2})^2; Re_i = \rho_f d_{p,i} \varepsilon_i |\mathbf{u}_i - \mathbf{v}_i| / \mu_f$$

$$\chi = 3.7 - 0.65 \cdot e^{-0.5(1,5 - \log(Re_i))^2}$$

Eq. 6: Drag force (Di Felice's model)

$$I_i \frac{d\omega_i}{dt} = \sum_{j=1}^{k_c} (M_{t,ij} + M_{r,ij})$$

Eq. 7: particles rotational momentum change

The forces of Basset, Saffman and Magnus are omitted for being several orders of magnitude lower than those considered in Eq. 3.

7) Conclusions

Observables calculated from an experiment carried out with RPT in a LSFB of alginate beads suspended in water have been compared to those estimated from CFD-DEM simulations.

Velocity fields, mixing times and solid dispersion coefficients are satisfactorily predicted.

[1] Salierno, G.L., Maestri, M., Piovano, S., Cassanello, M., Cardona, M.A., Hojman, D., Somacal, H., Calcium alginate beads motion in a foaming three-phase bubble column Chemical Engineering Journal 324 (2017) pp. 358-369

[2] Maestri, M.; Salierno, G.L.; Piovano, S.; Cassanello, M.C.; Cardona, M.A.; Hojman, D.; Somacal, H.: CFD-DEM modeling of solid motion in a water-calcium alginate fluidized column and its comparison with results from radioactive particle tracking, Chem. Eng. J. (2018) in press

References

The movement of fluids and solids in multiphase equipment was simulated with the open source CFDEM® software on Linux platform. Its use required obtaining the source code and compiling the components:

- OpenFOAM for the resolution of the Navier-Stokes equations of the fluid with the Solver Pressure-Implicit with Splitting of Operators (PISO), using k-ε model;
- LIGGGHTS for the simulation of the movement of 5000 solid particles, being implemented a uniform mesh on the order of 3 times the particle diameter;
- ParaView for the visualization of the results.

6) Results

- The liquid inlet distribution has a non-negligible effect on the predictive capacity of the simulations [2].
- The model reasonably predicts the solid phase distribution (Fig. 4 left) and dispersion coefficients once the steady state is attained [2].
- Fig. 5 shows the radial-axial projection of the solid velocities determined by azimuthally averaging the 3D velocity field.

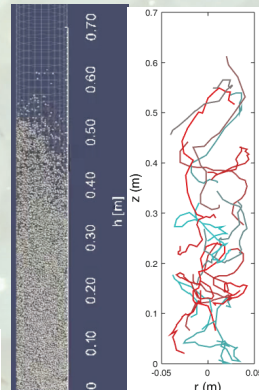


Fig. 4: Simulation of the LSFB (left) and trajectories acquired by RPT (right).

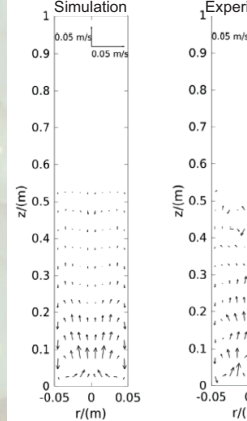


Fig. 5: Comparison of axial-radial velocity (time and azimuthally averaged; $u_r = 2$)

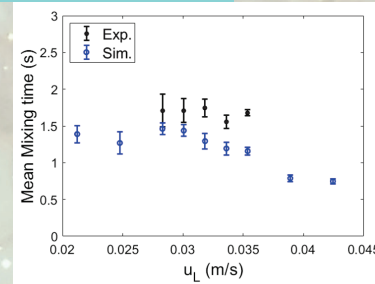


Fig. 6: Comparison of mixing times.

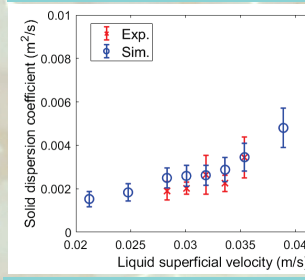


Fig. 7: Comparison of solid dispersion coefficient

Financial support from Universidad de Buenos Aires – UBA; Consejo Nacional de Investigaciones Científicas y Técnicas – CONICET and Agencia Nacional de Promoción Científica y Tecnológica – ANPCyT – is gratefully acknowledged.

Direction reversing active Brownian particle in a harmonic trap

Ion Santra

Abstract

We study the two-dimensional motion of an active Brownian particle of speed v_0 , with intermittent directional reversals—commonly observed among a large class of bacteria like *M. xanthus* and *P. putida*—in the presence of a harmonic trap of strength μ . The presence of the trap ensures that the position of the particle eventually reaches a steady state bounded within a circular region of radius v_0/μ , centered at the minimum of the trap. Due to the interplay between the rotational diffusion constant, reversal rate, and the trap strength, the steady state probability density shows a rich behaviour in the (D_R, γ, μ^{-1}) space, showing four qualitatively different types of shapes, which we refer to as active-I & II, and passive-I & II phases. In the active-I phase, the weight of the distribution is concentrated along an annular region close to the circular boundary, whereas in active-II, an additional central diverging peak appears giving rise to a Mexican hat-like shape of the distribution. The passive-I is marked by a single Boltzmann-like centrally peaked distribution in the large D_R limit. On the other hand, while the passive-II phase also shows a single central peak, it is distinguished from passive-I by a non-Boltzmann like divergence near the origin. We find the exact analytical forms of the distributions in various limiting cases and study the transitions between these phases. In particular, we show that for $D_R \ll \gamma$, the transition from active-II to passive-II occurs at $\mu = \gamma$. We compliment these analytical results with numerical simulations beyond the limiting cases and obtain a qualitative phase diagram in the (D_R, γ, μ^{-1}) space.

Reference: Direction reversing active Brownian particle in a harmonic potential, I Santra, U Basu, S Sabhapandit, arXiv:2107.12640 (2021)

Critical Behavior of the Ising Model under an external shear field: The Conserved Case

The non-equilibrium phase transitions of the two-dimensional magnetization-conserved Ising model under the action of an external shear field is investigated. This field, that simulates a convective velocity profile with shear rate γ , introduces anisotropic effects and forces the system to evolve into non equilibrium states. By employing the short-time dynamics (STD) methodology, it was possible to detect first- and second- order phase transitions, and in this last case the critical exponent were calculated. As a function of the absolute magnetization $|M|$ the system exhibits phase transitions of different order. On the one hand, If $|M|=0$, the model undergoes a second-order phase transition. The estimated critical temperature T_c depends on γ and two regimes can be distinguished: a power-law regime for low γ 's and a saturation regime at larger values of it. For the investigated shear field interval, the estimated values of the anisotropic critical exponents suggest that the critical behavior is on a crossover between the Ising and mean-field critical behaviors, respectively. On the other hand if $|M|> 0$, the model exhibits for each γ first-order phase transitions, ending in a critical point at $|M|=0$.

Nonequilibrium tricritical point in the Kuramoto model with additional nearest-neighbor interactions

The Kuramoto model serves as a paradigmatic framework to study the phenomenon of spontaneous collective synchronization. The usual Kuramoto model involves phase oscillators of distributed natural frequencies interacting via a mean-field interaction. In our present work, we study a variation of the model by including nearest-neighbor interactions on a one-dimensional periodic lattice. For unimodal and symmetric frequency distributions, we show that a competition between the two types of interactions brings in new features, and consequently, the resulting dynamics in the nonequilibrium stationary state exhibits a very rich phase diagram with both continuous and first-order transitions between synchronized and unsynchronized phases, with the transition lines meeting at a tricritical point. Our results are based on numerical integration of the dynamics as well as an approximate theory involving appropriate averaging of fluctuations in the stationary state. Reference: Mrinal Sarkar and Shamik Gupta, *Kuramoto model with additional nearest-neighbor interactions: Existence of a nonequilibrium tricritical point*, *Phys. Rev. E* 102, 032202 (2020).

Continuous quasi-attractors for irregular memories

Animals, like humans, navigate in complex territories. It is believed that mammals, at least, create cognitive maps of the environments they explore. The neurophysiological discovery of spatially selective cells in the hippocampal formation provided neuronal candidates involved in this capability. As a consequence, it has been hypothesized that the dynamics underlying the retrieval of environmental cognitive maps could be driven by continuous attractors, brittle mathematical objects which break with irregularities. However, the wilder the environment the more spatially selective cells seem to be activated unevenly. Can a continuous attractor theory contemplate also complex nonuniform activity? In this chapter we argue that it can, relaxing the requirement of a continuous manifold of fixed points to a quasi-attractive continuous manifold, intended as a direction of flow. We find that quasi-attractive manifolds persist under noise up to a critical value at which they abruptly break up. We show that some remarkably variable experimental recordings lie just at the edge of this transition.

Chaotic behavior of disordered nonlinear lattices

We focus on the mechanisms of energy transport in multidimensional heterogeneous lattice models, studying in particular the case of the Klein-Gordon model of coupled anharmonic oscillators in one and two spatial dimensions. We report the effects of the type of the impurity (heterogeneity) parameter on the systems' transport properties and classifies the transport mechanisms of the nonlinear versions of the models into various dynamical regimes. We also perform an extensive numerical investigation of the dynamics of the considered models revealing that for their nonlinear versions chaotic transport persists and chaotic hotspots meander in the region of energy concentration supporting the spreading mechanism.

Network Reconstruction from Data

Prediction of critical transitions can avert a lot of real-world problems such as heart attack or epilepsy crisis. Network reconstruction and prediction of critical transitions in a data-driven way is not just a learning problem because of parameter changes. The project aims to learn the evolution rule from the time series and then determine the network's topology using dynamical systems and statistical learning tools. In this numerical study, we mainly focus on the reconstruction of neural networks using a network obtained from the cerebral cortex image dataset of a mouse. We assume that we access measurement data from each node of this network as an application. On the other hand, we validate these learning tools on clinical data of cerebral vessels to predict the hemodynamic parameters.

Fluctuation-induced forces

They act on objects immersed in a fluctuating medium which constrain or modify its fluctuations (e.g. Casimir force in QED, Van der Waals and London forces...)

- Strength \propto energy of fluctuations ($\sim \hbar$ if quantum, $\sim k_B T$ if thermal)
- Range \propto range of the correlations

Can have [Casimir-like interactions](#) in a fluid close to a bulk [critical point!](#)

Minimal model

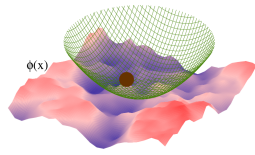
Optically trapped colloid immersed in a near-critical medium [1]

$$\mathcal{H} = \underbrace{\int d^d \mathbf{x} \left[\frac{1}{2} (\nabla \phi)^2 + \frac{1}{2} r \phi^2 \right]}_{\mathcal{H}_\phi} + \underbrace{\frac{k}{2} \mathbf{X}^2}_{\mathcal{H}_X} - \lambda \underbrace{\int d^d \mathbf{x} \phi(\mathbf{x}) V(\mathbf{x} - \mathbf{X})}_{\mathcal{H}_{int}^Z}$$

Dynamics:

$$\begin{aligned} \dot{\mathbf{X}}(t) &= -\nu \nabla_{\mathbf{X}} \mathcal{H} + \boldsymbol{\xi}(t) \\ \partial_t \phi(\mathbf{x}, t) &= -D(i\nabla)^{\alpha} \frac{\delta \mathcal{H}}{\delta \phi(\mathbf{x}, t)} + \zeta(\mathbf{x}, t) \end{aligned}$$

in a thermal bath @ T and satisfying FDT,



$$\begin{aligned} \langle \xi_i(t) \xi_j(t') \rangle &= 2\nu T \delta_{ij} \delta(t-t') \\ \langle \zeta(\mathbf{x}, t) \zeta(\mathbf{x}', t') \rangle &= 2DT (i\nabla)^{\alpha} \delta^d(\mathbf{x} - \mathbf{x}') \delta(t-t') \end{aligned}$$

In equilibrium,

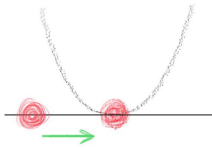
$$P_{eq}(\mathbf{X}) \propto \int \mathcal{D}\phi e^{-\beta \mathcal{H}(\phi, \mathbf{X})} \propto e^{-\beta U_X}$$

but what happens out of equilibrium?

Relaxation towards equilibrium

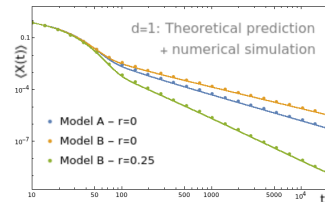
Perturbative analysis in λ :

$$\begin{aligned} \mathbf{X}(t) &= \sum_n \lambda^n \mathbf{X}^{(n)}(t) \\ \phi(\mathbf{x}, t) &= \sum_n \lambda^n \phi^{(n)}(\mathbf{x}, t) \end{aligned}$$



The leading correction shows a [power-law](#) decay close to criticality, also observed in numerical simulations:

$$\langle X^{(2)}(t) \rangle \sim \begin{cases} t^{-(1+\frac{\alpha}{2})}, & \text{Model A, } r=0 \\ t^{-(1+\frac{\alpha}{2})}, & \text{Model B, } r=0 \\ t^{-(2+\frac{\alpha}{2})}, & \text{Model B, } r>0 \end{cases}$$



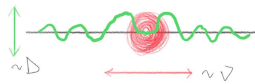
Adiabatic approximation

In Fourier space,

$$\begin{aligned} \dot{\mathbf{X}}(t) &= -\nu k \mathbf{X}(t) + \nu \lambda \int_{\mathbf{R}} \frac{d^d q}{(2\pi)^d} i \mathbf{q} V_{-q} \phi_q(t) e^{i \mathbf{q} \cdot \mathbf{X}(t)} + \boldsymbol{\xi}(t) \\ \dot{\phi}_q^{R,I}(t) &= -Dq^{\alpha}(q^2 + r) \phi_q^{R,I}(t) + \lambda Dq^{\alpha} V_q \left[e^{-i \mathbf{q} \cdot \mathbf{X}(t)} \right]^{R,I} + \zeta_q^{R,I}(t) \end{aligned}$$

Field modes are:

- decoupled
- fast variables for large D .



Using [adiabatic elimination](#) we obtain

$$\partial_t P(\mathbf{X}, t) = \mathcal{L}_X^{\text{eff}} P(\mathbf{X}, t)$$

where in the case of an isotropic interaction potential

$$\mathcal{L}_X^{\text{eff}} = \chi \left\{ \nabla \cdot (\nu k \mathbf{X}) + \nu T \nabla^2 \right\} + \mathcal{O}\left(\frac{1}{D^2}\right), \quad \chi \equiv 1 - \frac{\lambda^2 \nu}{Dd} \int_{\mathbf{R}} \frac{d^d q}{(2\pi)^d} \frac{q^{2-\alpha}}{(q^2 + r)^2} |V_q|^2$$

unable to describe algebraic relaxation!

A matter of timescales

Relaxation timescales are set by the trap strength and by the field correlation length $\xi \sim r^{-2}$, which diverges at criticality ($r=0$):

$$\begin{aligned} \tau_X^{-1} &= \nu k \\ \tau_\phi^{-1} &= Dq^{\alpha}(q^2 + r) \end{aligned}$$

Any adiabatic approach fails when $\tau_\phi \gg \tau_X$: beware of slow modes close to $r=0$!

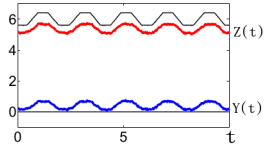
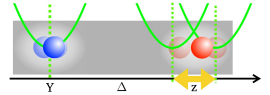
Forced oscillations (NESS)

Model:

$$\mathcal{H} = \mathcal{H}_\phi + U_Y + U_Z - \lambda \left\{ \mathcal{H}_{int}^Y + \mathcal{H}_{int}^Z \right\}$$

Colloid \mathbf{Z} is trapped in a stiff moving trap,

$$\begin{aligned} \mathcal{H}_Z &= \frac{k_z}{2} [\mathbf{Z} - \mathbf{Z}_F(t)]^2 \\ \mathbf{Z}_F(t) &= \Delta + \mathbf{A} \sin(\Omega t) \end{aligned}$$



Experiments [2] show colloid \mathbf{Y} to start moving if the surrounding medium (e.g. a binary mixture) gets close to a [continuous PT](#).

Master equation

In the NESS, we can derive perturbatively

$$\partial_t P_1(\mathbf{y}, t) = \mathcal{L}_0 P_1(\mathbf{y}, t) + \lambda^2 \mathcal{L}_2(t) P_1(\mathbf{y}, t) + \mathcal{O}(\lambda^3)$$

where

$$\begin{aligned} \mathcal{L}_0 &= \nabla_{\mathbf{y}} \cdot (\nu k \mathbf{y} + \nu T \nabla_{\mathbf{y}}) \\ \mathcal{L}_2(t) &= \nabla_{\mathbf{y}} \cdot \nu \int \frac{d^d q}{(2\pi)^d} i \mathbf{q} |V_q|^2 e^{-i \mathbf{q} \cdot \mathbf{y}} \int_{t_0}^t ds \chi_q(t-s) e^{i \mathbf{q} \cdot \mathbf{Z}(s)} \end{aligned}$$

and $\chi_q(t-s)$ is the dynamical field susceptibility.

This can be used to obtain the full [moment generating function](#).

Adiabatic approach

At equilibrium, the joint distribution is canonical

$$\mathcal{P}(\mathbf{Y}, \mathbf{Z}) = e^{-\beta(\mathcal{H}_\phi + \mathcal{H}_Z)} \int \mathcal{D}\phi e^{-\beta(\mathcal{H}_\phi - \lambda \mathcal{H}_{int})} \propto e^{-\beta\{\mathcal{H}_\phi + \mathcal{H}_Z - \lambda^2 V_c(\mathbf{Y}, \mathbf{Z})\}}$$

with the induced [interaction potential](#)

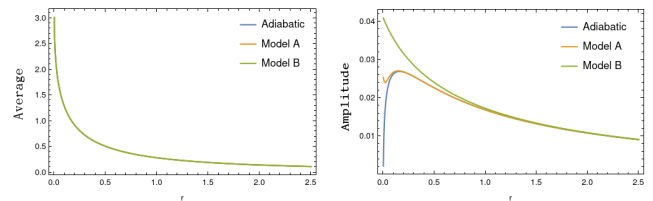
$$V_c(\mathbf{Y}, \mathbf{Z}) = \int \frac{d^d q}{(2\pi)^d} \frac{|V_q|^2}{q^2 + r} e^{i \mathbf{q} \cdot (\mathbf{Z} - \mathbf{Y})}$$

We can write an [effective EOM](#) pretending we are at equilibrium, instead by instant:

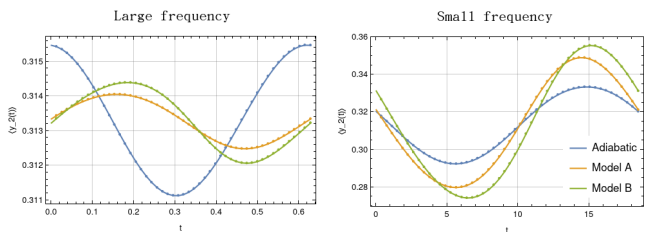
$$\dot{\mathbf{Y}}_{eq}(t) = -\nu \nabla_{\mathbf{y}} \left[\mathcal{H}_y - \lambda^2 V_c(\mathbf{Y}, \mathbf{Z}) \right] + \boldsymbol{\xi}(t)$$

Comparison

Using harmonic analysis,



The dynamical amplitude may be bigger or smaller than its adiabatic prediction,



but there exists a value of r such that the system becomes effectively adiabatic:

$$\begin{cases} \tau_\phi^{-1} \sim Dq^{\alpha}(q^2 + r) \\ \tau_\Omega^{-1} \sim \Omega \end{cases} \Rightarrow r_A \sim \Omega, \quad r_B \sim \Omega^{\frac{1}{2}}$$

References

- U. Basu, V. Démery, and A. Gambassi. Dynamical behavior of a colloidal particle surfing a critical gaussian field. *In preparation*.
- Ignacio A. Martinez, Clemence Devailly, Artyom Petrosyan, and Sergio Ciliberto. Energy transfer between colloids via critical interactions. *Entropy*, 19(2), 2017.

P41

Dragged colloids in (active) fields

Probability density of bipolaron in a parabolic potential two-dimensional quantum dot under external magnetic and electric fields

In this article, we study the probability of the presence of electrons at any point in space in a parabolic potential quantum dot under the effect of an external magnetic and electric fields. The ground state and the first excited state energies were evaluated using the Pekar-type variational method. Numerical calculations indicate that the application of electric and magnetic fields have effects on the properties of the bipolaron. We also observed that when the system is in the presence of both fields electric and magnetic, the probability of the appearance of the two electrons near the center of the quantum point is greater. In addition, we found that for some values of both fields in the system, we can better control the bipolaron and we can also be able to obtain some polaronic behavior.

Distinguished correlation properties of Chebyshev dynamical systems

We study distinguished correlation properties of a family of shifted Chebyshev maps $T_{\{N, a\}}$, present analytic results for two-point and higher-order correlation functions and show that $T_{\{N, 0\}}$ are most random-like among all smooth 1D maps conjugated to a Bernoulli shift of N symbols, in the sense that they have least higher-order correlations. Results for eigenfunctions of the transfer operator for Chebyshev maps are also reviewed. We further consider coupled map lattices of shifted Chebyshev maps and numerically investigate zeros of the temporal and spatial nearest-neighbour correlations, which are of interest in chaotically quantised field theories and other spatially extended systems. [Chaos, Solitons & Fractals: X Vol.5, 100035 (2020)]



Solving the Poles of Nonextensive Statistical Physics

D.J. Zamora^{1,2}

1. Centro Brasileiro de Pesquisas Físicas (CBPF) and Instituto Nacional de Ciência e Tecnologia de Sistemas Complexos (INCT-SC), Rio de Janeiro, Brazil.
 2. Instituto de Física del Noroeste Argentino (INFNOA); UNT-CONICET, Tucumán, Argentina. javierzamora055@gmail.com



1. Introduction In order to statistically describe the dynamics of a plethora of complex systems, nonextensive statistics has been proposed in [1]. In the last decades, this new generalized statistical mechanical formalism have found a large variety of very successful applications, even beyond the realm of physics. It was found in [2] that classical Tsallis' theory exhibits poles in the partition function and the mean energy. This occurs at a countable set of the q -line. I give a mathematical account of them. Further, by focusing attention upon the pole, one encounters interesting effects. The study and elimination of divergences of a physical theory is perhaps one of the most important aspects of theoretical physics nowadays. I propose two different approaches to solve those divergences: i - a perturbative approximation [3], useful for the weak non-additive limit, and ii - dimensional regularization [4]. The partition function and the mean energy in the nonextensive framework are defined as:

$$Z = \int [1 + (q-1)\beta H(p, x)]^{\frac{1}{1-q}} dp dx \quad (1)$$

$$U = \frac{1}{Z} \int H(p, x) [1 + (q-1)\beta H(p, x)]^{\frac{1}{1-q}} dp dx \quad (2)$$

Where p is the momentum, x the coordinate, β the inverse temperature, H the Hamiltonian, and q a real parameter. The limit $q=1$ recover the usual statistics. I will show here their divergences by appealing to two very different examples: a harmonic oscillator and the gravitational potential.

2. Harmonic Oscillator-like Hamiltonian

I just show results for the partition function here but the mean energy usually shares the same poles.

Let us take $H(p, x) = p^2 + x^2$, where p^2 and x^2 have dimensions of energy. The solution of eq. (1) in v dimensions is [2]:

$$Z = \frac{\pi^v}{[\beta(q-1)]^v} \frac{\Gamma(\frac{1}{q-1} - v)}{\Gamma(\frac{1}{q-1})} \quad (3)$$

The singularities are given by the poles of the Γ function, i.e., for:

$$\frac{1}{q-1} - v = -n \quad \text{for } n = 0, 1, 2, \dots \quad (4)$$

Or $q = 2, \frac{3}{2}, \frac{4}{3}, \frac{5}{4}, \dots$. Represented in figure 1 for the cases $v=1$, $v=2$ and $v=3$.

The poles are not a particularity of this Hamiltonian, as I will show next.

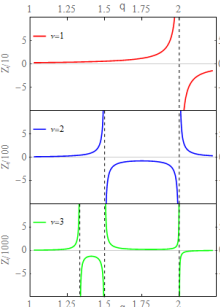
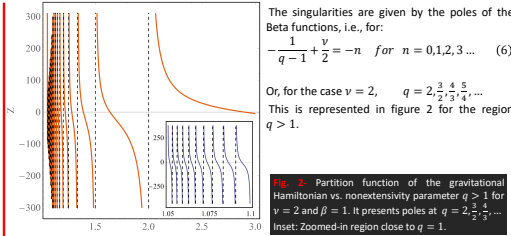


Fig. 1. Partition function of the harmonic oscillator vs nonextensivity parameter q for different dimensions and $\beta = 1$. It can be appreciated the poles at $q = 2, \frac{3}{2}, \frac{4}{3}, \dots$

3. Gravitational Hamiltonian

Let us consider a particle of mass m under the influence of the Newtonian gravitational potential of a mass $M \gg m$. The Hamiltonian reads $H(p, x) = \frac{p^2}{2m} - \frac{GMm}{r}$. The solution of eq. (1) in v dimensions for this case is [4]:

$$Z = \frac{2[2\pi^2\beta(q-1)G^2M^2m^3]^{\frac{1}{2}}}{\Gamma^2(\frac{v}{2})} B\left(\frac{v}{2}, \frac{1}{q-1} + 1\right) B\left(\frac{v}{2} + \frac{1}{1-q}, -v\right) \quad (5)$$



The singularities are given by the poles of the Beta functions, i.e., for:

$$-\frac{1}{q-1} + \frac{v}{2} = -n \quad \text{for } n = 0, 1, 2, 3, \dots \quad (6)$$

Or, for the case $v=2$, $q = 2, \frac{3}{2}, \frac{4}{3}, \dots$. This is represented in figure 2 for the region $q > 1$.

Fig. 2. Partition function of the gravitational Hamiltonian vs nonextensivity parameter $q > 1$ for $v=2$ and $\beta = 1$. It presents poles at $q = 2, \frac{3}{2}, \frac{4}{3}, \dots$. Inset: Zoomed-in region close to $q = 1$.

4. Avoiding divergences: approximation

When working out with the nonextensive statistical mechanics of a given system, the divergences of the partition function and the mean energy can lead to useful results. Consider, for example, one wants to study the thermostatics of a system. One could restricts the domain and work in the well-defined region between two consecutive divergences. However, suppose one wants to study the behaviour of the system in the region close to the extensive limit ($q = 1$), which is the case of several important applications in nonextensive statistics. The previous examples illustrate the fact that, when approaching to the limit, the poles appear more often.

A way to avoid divergences is to use an approximation instead of the Tsallis' entropy. This is based on a first order expansion of the q -exponential function around a particular value of the nonextensivity parameter, for example, $q = 1$.

$$[1 + (1-q)x]^{1/(1-q)} \approx \left[1 + \frac{(1-q)x^2}{2}\right] e^{-x} \quad (7)$$

In [3] we demonstrate that this 'new entropy' does not present poles and a MaxEnt process can be performed leading to:

$$Z = \int \left[1 + \frac{(1-q)(BH)^2}{2}\right] e^{-BH} dp dx \quad (8)$$

The approximation is quite good for small values of the argument. The fig. 3 shows the ratio R between the approximated and exact solution.

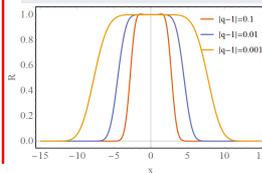


Fig. 3. Ratio R between approximate and exact solution to the MaxEnt process vs argument x and different values of q close to 1.

Of course one can improve the approximation as much as one desires by taking more terms in the expansion, but making the calculus more complicated.

5. Solving divergences: Dimensional Regularization

A more exact and intricate calculus involve solving the poles through dimensional regularization (DR). It constitutes perhaps one of the most important theoretical physics advances in the last decades. A more detailed explanation can be founded in [4].

To practical aims, the idea is that if we have, for instance, a function $F(v)$ depending of the dimension v , we perform the Laurent-expansion of $F(v)$ around the desired dimension v_0 and select afterward, as the physical result, the v_0 -independent term.

For example, going back to eq. 5, we can particularize for $q = 3/2$ and applying the DR procedure for $v = 3$ we obtain:

$$Z = \frac{4\pi^2}{3} (\beta G^2 M^2 m^3)^{\frac{3}{2}} \frac{23}{3} - \ln(16\pi^2 \beta G^2 M^2 m^3)$$

This procedure leads to some coherent results, such as negative specific heats, in accordance with that astronomers knew about the specific heat of self-gravitational systems. Figure 4 shows the dimensionless specific heat for the system considered here. It can be appreciated also that a lower bound exists for the temperature of the system.

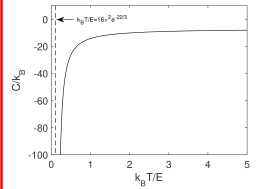


Fig. 4. Dimensionless specific heat versus $k_B T/E$ for $q = 3/2$, where $E = G^2 M^2 m^3$. Specific heat is negative, as befits gravitation.

Highlights

The poles of some main measures of nonextensive statistics are presented by appealing to two examples.

The first example is the partition function of an Harmonic Oscillator-like Hamiltonian.

The second example is a particle in a gravitational potential. The partition function presents infinite poles in the q -line.

Two approaches are proposed to solve the poles.

The first approach is an approximation which allow us to avoid the divergences at the expense of losing exactitude.

The second approach involves using the dimensional regularization technique. This solves the divergence for a particular value of the nonextensivity parameter.

References
 [1] C. Tsallis: Journal of Statistical Physics 52.1-2 (1988), pp. 47-487.
 [2] A. Plastino and M. C. Rocca: EPL (Europhysics Letters) 104.6 (2013), p. 60003.
 [3] G.L. Ferri et al., The European Physical Journal B 90.3 (2017).
 [4] D.J. Zamora et al., Physica A 497 (2018), pp. 310-318.

Acknowledgment: CAPES and CONICET